Quantum dynamics of a plane pendulum

Monika Leibscher[1] and Burkhard Schmidt[2]

[1]*Institut für Chemie und Biochemie, Freie Universität Berlin, Takustr. 3, D–14195 Berlin, Germany*[*]

[2]*Institut für Mathematik, Freie Universität Berlin, Arnimallee 6, D–14195 Berlin, Germany*[†]

(Dated: March 27, 2009)

Abstract

A semi-analytical approach to the quantum dynamics of a plane pendulum is developed, based on Mathieu functions which appear as stationary wave functions. The time-dependent Schrödinger equation is solved for pendular analogues of coherent and squeezed states of a harmonic oscillator, induced by instantaneous changes of the periodic potential energy function. Coherent pendular states are discussed between the harmonic limit for small displacements and the inverted pendulum limit, while squeezed pendular states are shown to interpolate between vibrational and free rotational motion. In the latter case, full and fractional revivals as well as spatiotemporal structures in the time-evolution of the probability densities (quantum carpets) are quantitatively analyzed. Corresponding expressions for the mean orientation are derived in terms Mathieu functions in time. For periodic double well potentials, different revival schemes and different quantum carpets are found for the even and odd initial states forming the ground tunneling doublet. Time evolution of the mean alignment allows the separation of states with different parity. Implications for external (rotational) and internal (torsional) motion of molecules induced by intense laser fields are discussed.

[*]E-mail: monika@chemie.fu-berlin.de

[†]E-mail: burkhard.schmidt@fu-berlin.de

I. INTRODUCTION

A plane pendulum in classical physics can be realized by a point mass particle restricted to move on a circle, subject to a trigonometric, proportional to $\cos\theta$, potential energy function in the angular coordinate θ. The quantum pendulum can be realized in molecular physics where the external degrees of freedom can be manipulated by electric fields. For example, linear molecules can be oriented or aligned by interaction with their permanent dipoles [1] or induced dipoles [2–5], respectively. Other applications of the pendulum in the realm of molecules involve internal rotation of molecules [6], e. g., the torsion of the two methyl groups comprising an ethane molecule [7]. Yet another example for the realization of a microscopic pendulum are cold atoms in an optical lattice [8], which is formed by counter propagating laser beams. In this atom optics realization of a quantum pendulum [9, 10], the spatial squeezing of the atoms is analogous to the orientation of a rotor [11].

Soon after its first formulation, the stationary Schrödinger equation has been solved for the plane pendulum by E. U. Condon [12]. Despite of its fundamental importance, this solution is barely mentioned in textbooks [13], probably because the wave functions are Mathieu functions which were first discussed in the context of vibrations of an elliptic membrane [14]. Although Mathieu's functions cannot be given as analytical expressions, there exists an extensive body of literature on the numerical analysis of these functions [15–18]. Depending on the energies considered, the plane pendulum can be regarded as an interpolation between two exactly soluble limiting cases [7, 19]: For energies well below the potential barrier, pendular states approach the (non-degenerate) states of a harmonic oscillator with equally spaced energy levels. For the high energy limit, pendular states approach the (doubly-degenerate) eigen states a free rotor with quadratically spaced energy levels.

With very few exceptions [20–23] , the quantum dynamics of plane pendular states is a largely unexplored field. This situation is in marked contrast to the two limiting cases of the pendulum: For the harmonic oscillator, there is a substantial body of literature, particularly on the celebrated coherent and squeezed states representing the closest quantum analogue to classical vibrational dynamics [24–26]. For the free rotor and for the closely related particle in a box, the quantum dynamics is subject to pronounced quantum effects. In general, the non-linear energy level progressions give rise to (fractional) revivals and super-

revivals. The revival theory is based on the fact that long time wavepacket dynamical phenomena are directly encoded in the energy representation of multi-level quantum systems [27–31]. A special case represents the particle in a box with its quadratic energy spectrum analyzed, e. g., in Ref. [32]. In addition to the purely temporal structures of (fractional) revivals, intriguing patterns have been found in the correlated space-time dependence of wave functions and probability densities. The structures of these so-called quantum carpets have been thoroughly analyzed in Refs. [33, 34]

The present work aims at an in-depth investigation of time-dependent phenomena of the quantum pendulum. In particular, pendular analogues of squeezed and coherent state of harmonic oscillators shall be studied. To this end, we consider the quantum dynamics of pendular states induced by an instantaneous change of barrier height or by an instantaneous shift of the trigonometric potential, respectively. In the former case, the quantum dynamics of squeezed pendular states naturally connects the limits of the harmonic oscillator and the free particle on a ring [21]. In the latter case, the quantum dynamics of coherent pendular states shall be shown to lie between the harmonic oscillator and the inverted pendulum limit [20]. Other interesting features in pendular quantum dynamics arise for a $\cos(2\theta)$ potential, which can be regarded as a periodic analogue of a double well potential. Apart from quantum rotation tunneling [22] leading to splitting of low-lying energy levels, interesting effects on the wave packet dynamics are expected to arise from the even or odd parity of the initial states. Note that the anti-symmetry principle relates rotational eigen states with even and odd parity to nuclear spin isomers. Recently, it has been demonstrated that laser induced alignment of linear molecules [35] and intramolecular torsion of rotatable molecules can be used to select nuclear spin states [36].

In our studies of pendular quantum dynamics, our attention shall focus on two aspects. First, the dependence of the wave packet dynamics on the nature of the initial (squeezed or coherent) pendular state will be investigated: In particular, different interference schemes are expected to lead to different (fractional) revivals and to different patterns in the space-time densities (quantum carpets). Note that approximate expressions for the corresponding revival times in the vicinity of the harmonic oscillator and the free rotor limit have been derived by perturbation theory [23]. Second, the influence of the initial state on the expectation values of observables shall be monitored. In particular, we want to calculate and discuss the mean orientation and mean alignment versus time for various quantum dynamical sce-

narios. In this way, the present article is related to recent work on field-free alignment of molecules, induced by non-resonant interaction with strong laser fields [5, 37]. In particular, the instantaneous switches involved in the definition of squeezed and/or coherent states [26] have been realized in molecular alignment experiments by means of adiabatic turn-on and sudden turn-off of the laser field [38, 39].

II. STATIONARY PENDULAR STATES

Before we discuss the quantum dynamics of the plane pendulum, let us first review its stationary quantum states. The dimensionless Hamiltonian operator in units of twice the rotational constant $2B = \hbar^2/I$ is given by

$$\hat{H} = -\frac{1}{2}\frac{d^2}{d\theta^2} + \frac{V}{2}[1 + \cos(m\theta)] \tag{1}$$

where $0 \leq \theta \leq 2\pi$ denotes the angular variable, I stands for the moment of inertia, and the potential energy function has m minima separated by m barriers of height $V > 0$. The corresponding time-independent Schrödinger equation $\hat{H}\phi = E\phi$ is equivalent to the Mathieu equation

$$\frac{d^2\phi_n}{d\eta^2} + (a_n - 2q\cos 2\eta)\phi_n = 0 \tag{2}$$

for scaled angle $\eta = m\theta/2$ and scaled barrier height $q = 2V/m^2$. Then the pendular eigen energies E are related to the characteristic values a of Mathieu's equation through

$$E_n = \frac{m^2}{8}a_n + \frac{V}{2} \tag{3}$$

thus revealing an interesting scaling property for wave functions with periodicity $2\pi/m$ of the plane quantum pendulum: A change of the multiplicity from m to m' accompanied by a change from V to $V' = (m'/m)^2 V$ implies the following changes in the angles, energies, and time

$$\theta' = \frac{m}{m'}\theta, \quad E' = \left(\frac{m'}{m}\right)^2 E, \quad t' = \left(\frac{m}{m'}\right)^2 t \tag{4}$$

which serves useful in our later considerations of the free rotor limit ($V = V' = 0$) of pendular states. The required 2π–periodicity $\phi_n(\theta + 2\pi) = \phi_n(\theta)$ in the original angular coordinate θ translates to $m\pi$–periodicity $\phi_n(\eta + m\pi) = \phi_n(\eta)$ in the reduced coordinate η. Appropriate solutions are obtained as Mathieu's cosine elliptic (ce) or sine elliptic (se)

functions [15–17], respectively,

$$\phi_{2n}(\eta) \;=\; \frac{1}{\sqrt{\pi}}\mathrm{ce}_{\frac{2n}{m}}\left(\eta;q\right) \tag{5a}$$

$$\phi_{2n+1}(\eta) \;=\; \frac{1}{\sqrt{\pi}}\mathrm{se}_{\frac{2n+2}{m}}\left(\eta;q\right) \tag{5b}$$

with $n \geq 0$. For a regular pendulum with a single potential well, $m = 1$, these wave functions can be expressed as a Fourier series in the original variables θ, V (with $\eta = \theta/2$ and $q = 2V$)

$$\phi_{2n}(\theta) \;=\; \frac{1}{\sqrt{\pi}}\mathrm{ce}_{2n}\left(\frac{\theta}{2};2V\right) = \frac{1}{\sqrt{\pi}}\sum_{k=0}^{\infty} A_k^{(2n)}\cos(k\theta) \tag{6a}$$

$$\phi_{2n+1}(\theta) \;=\; \frac{1}{\sqrt{\pi}}\mathrm{se}_{2n+2}\left(\frac{\theta}{2};2V\right) = \frac{1}{\sqrt{\pi}}\sum_{k=1}^{\infty} B_k^{(2n+1)}\sin(k\theta) \tag{6b}$$

Note that only even order se or ce functions occur because the above-mentioned requirement of periodicity. The discrete Fourier coefficients on the right hand side are given by

$$A_0^{(2n)} \;=\; \frac{1}{2\sqrt{\pi}}\int_0^{2\pi}\phi_{2n}(\theta)\,d\theta \tag{7a}$$

$$A_k^{(2n)} \;=\; \frac{1}{\sqrt{\pi}}\int_0^{2\pi}\phi_{2n}(\theta)\,\cos(k\theta)\,d\theta \tag{7b}$$

$$B_k^{(2n+1)} \;=\; \frac{1}{\sqrt{\pi}}\int_0^{2\pi}\phi_{2n+1}(\theta)\,\sin(k\theta)\,d\theta \tag{7c}$$

with $k > 0$. The traditional way of calculating the characteristic values a_n and, hence, the energies E_n and the corresponding coefficients A, B employs recursive methods of continued fractions [15, 16]. However, this approach tends to become unstable for large barrier heights. Instead, we resort to the Fourier grid Hamiltonian method which was proposed for general potential energy functions in Refs. [40, 41] and in the special context of periodic potentials and Mathieu functions in Ref. [18]. Inserting the Fourier series (6) into the Mathieu equation (2) yields an eigenvalue problem with a symmetric tri-diagonal representation of the Hamiltonian (1) which is routinely solved e. g. by the LAPACK package implemented in MATLAB. The numerical effort scales with $\mathcal{O}(N\log_2 N)$ where N is the number of basis functions.

Useful illustrations of Mathieu functions are compiled in Ref. [17] which shall not be reproduced here. In analogy to extensive work on orientation ($m = 1$) and alignment ($m = 2$) of linear molecules interacting with external fields [42], stationary wave functions

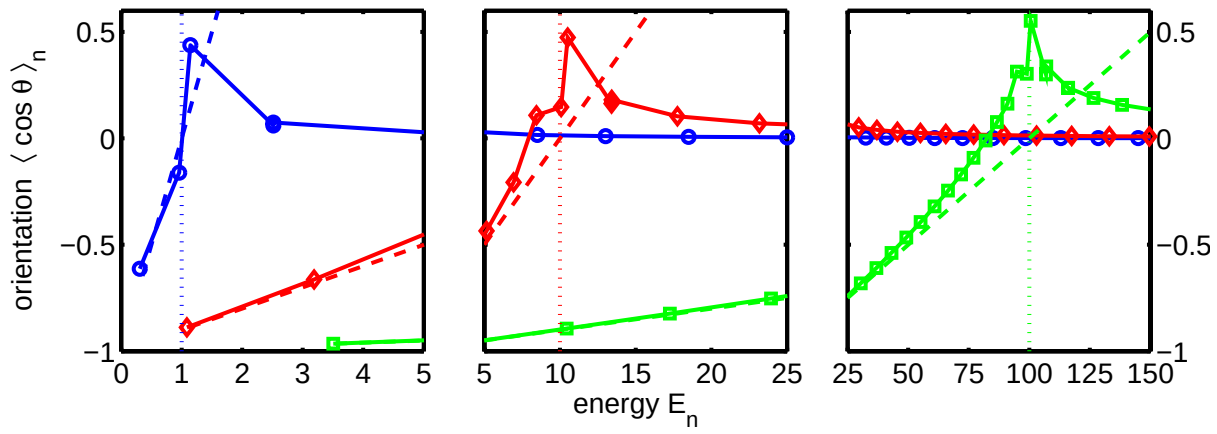

FIG. 1: Expectation values of orientation $\langle \cos\theta \rangle_n$ for stationary pendular states with $V = 1$ (blue circles), $V = 10$ (red diamonds) and $V = 100$ (green squares), as indicated by the vertical, dotted lines. The corresponding harmonic oscillator limits (13) are represented by dashed lines.

on a circular domain shall be characterized here and throughout this work by the following mean (expectation) value of $\cos^m\theta$which is closely related to the partitioning of kinetic and potential energy via Eq. (1). For the first case to be investigated here ($m = 1$),

$$\langle \cos\theta \rangle_{2n} = \int_0^{2\pi} |\phi_{2n}(\theta)|^2 \cos\theta \, d\theta = A_0^{(2n)} A_1^{(2n)} + \sum_{k=0}^{\infty} A_k^{(2n)} A_{k+1}^{(2n)} \tag{8a}$$

$$\langle \cos\theta \rangle_{2n+1} = \int_0^{2\pi} |\phi_{2n+1}(\theta)|^2 \cos\theta \, d\theta = \sum_{k=1}^{\infty} B_k^{(2n+1)} B_{k+1}^{(2n+1)} \tag{8b}$$

where only successive terms of the Fourier series expansion (6) are coupled.

Fig. 1 shows typical results for the mean orientation of stationary pendular states: For sufficiently small quantum number n with $E_n \ll V$, the wave functions are essentially confined to the region of the potential minimum at $\theta = \pi$ resulting in highly oriented pendular states with $\langle \cos\theta \rangle \approx -1$, see subsection A on the harmonic oscillator limit. At intermediate values of n, the energies approach the barrier height $E_n \approx V$ and the wave functions exhibit large amplitudes in the region of the potential maximum, thus leading to moderate anti–orientation with $\langle \cos\theta \rangle \approx 0.5$. Finally, in the limit of large quantum numbers, $n \to \infty$ with $E_n \gg V$, the wave functions approach simple cosine or sine functions and the mean orientation converges to zero, see subsection B on the free rotor limit.

A. Harmonic oscillator limit

When the energies of pendular states are well below the barrier height ($E \ll V$), the Hamiltonian (1) for the trigonometric potential energy function with $m = 1$ can be replaced by its harmonic approximation

$$\hat{H} = -\frac{1}{2}\frac{d^2}{d\xi^2} + \frac{V}{4}\xi^2 \tag{9}$$

for small values of the displacement coordinate $\xi = \theta - \pi$. The corresponding eigen energies and functions for the harmonic oscillator are

$$E_n = \left(n + \frac{1}{2}\right)\beta^2, \quad \phi_n(\xi) = N_n\, H_n(\beta\xi)\, \exp\left(-\frac{\beta^2\xi^2}{2}\right) \tag{10}$$

with $n \geq 0$, the parameter $\beta \equiv (V/2)^{1/4}$ and H_n being Hermite polynomials. The correct normalization of the wave functions, $\int_{-\infty}^{+\infty} |\phi_n(\xi)|^2 d\xi = 1$, is ensured by

$$N_n = \left(\frac{\beta^2}{\pi}\right)^{1/4} \frac{1}{(2^n n!)^{1/2}} \tag{11}$$

In order to adapt the wave functions for even or odd quantum number to the periodic boundary conditions of the pendulum, a discrete cosine or sine Fourier transformation (7), respectively, is performed for the harmonic oscillator limit, $\beta \to \infty$, yielding the following coefficients [16]

$$A_0^{(2n)} = (-1)^n \frac{1}{\sqrt{2}}\frac{N_{2n}}{\beta} H_{2n}(0) = \frac{2^n}{\sqrt{2}}\frac{N_{2n}}{\beta}(2n-1)!! \tag{12a}$$

$$A_k^{(2n)} = (-1)^{k+n}\sqrt{2}\frac{N_{2n}}{\beta}\exp\left(-\frac{k^2}{2\beta^2}\right) H_{2n}\left(\frac{k}{\beta}\right) \tag{12b}$$

$$B_k^{(2n+1)} = (-1)^{k+n}\sqrt{2}\frac{N_{2n+1}}{\beta}\exp\left(-\frac{k^2}{2\beta^2}\right) H_{2n+1}\left(\frac{k}{\beta}\right) \tag{12c}$$

for $k > 0$ and $n \geq 0$ and where the double factorial is defined as $(2n-1)!! = 1\cdot 3\cdot 5 \cdots (2n-1)$.

In the harmonic limit, the expectation value of the orientation of a pendulum can be approximated by a truncated Taylor expansion of the cosine function around the minimum at $\xi = \theta - \pi = 0$

$$\langle \cos\theta \rangle_n \approx -1 + \frac{1}{2}\langle \xi^2 \rangle_n = -1 + \frac{1}{2}\left[(\delta\xi_n)^2 + \langle \xi \rangle_n^2\right] \tag{13}$$

with the position uncertainty (fluctuation) for the standard harmonic oscillator $(\delta\xi_n)^2 = (2n+1)/(2\beta^2)$ and $\langle \xi \rangle = 0$. As indicated by the dashed lines in Fig. 1, the linear relation is in good agreement with the numerical result for the Mathieu function for low quantum

numbers with $E_n < V$, while there are major deviations for higher n. Evidently, the figure shows that the range of validity of the harmonic approximation increases with increasing barrier height V.

B. Free rotor limit

For vanishing barrier height ($V \to 0$), the Hamiltonian (1) approaches that of a free particle on a ring

$$\hat{H} = -\frac{1}{2}\frac{d^2}{d\theta^2} \tag{14}$$

The eigenvalues for $n > 0$ are doubly degenerate with corresponding even and odd eigenfunctions which are simply proportional to cosine and sine trigonometric functions, respectively,

$$E_0 = 0, \qquad \phi_0(\theta) = \frac{1}{\sqrt{2\pi}} \tag{15a}$$

$$E_{2n} = \frac{n^2}{2}, \qquad \phi_{2n}(\theta) = \frac{1}{\sqrt{\pi}}\cos(n\theta) \tag{15b}$$

$$E_{2n+1} = \frac{n^2}{2}, \qquad \phi_{2n+1}(\theta) = \frac{1}{\sqrt{\pi}}\sin(n\theta) \tag{15c}$$

for $n > 0$ with trivial Fourier coefficients

$$A_0^{(2n)} = \frac{1}{\sqrt{2}}\,\delta_{n,0} \tag{16a}$$

$$A_k^{(2n)} = B_k^{(2n+1)} = \delta_{k,n} \tag{16b}$$

for $k > 0$ and $n \geq 0$ and where δ stands for Kronecker's symbol.

In the free rotor limit, the expectation value of the orientation of a pendulum vanishes exactly due to the symmetry of the wave function, see Eq. (8). This is also illustrated in Fig. 1. For the lowest barrier height considered ($V = 1$), we find $\langle \cos\theta \rangle_n \approx 0$ for all but the very lowest quantum numbers n. Obviously, the range of validity of the free rotor approximation decreases with increasing barrier height V.

III. PENDULAR ANALOGUE OF SQUEEZED STATE

In this section we consider the generalization of the squeezed state to a periodic situation with a trigonometric potential, see Eq. (1). In analogy to the situation for a harmonic

oscillator [26], squeezed states can be created by a sudden change of the barrier height from V to $\tilde{V}$. We aim at solutions of the time-dependent Schrödinger equation $i\partial_t\psi(t) = \hat{H}\psi(t)$ where the dimensionless time is given in units of $1/(2B) = I/\hbar$ and where the initial wave function is chosen to be the lowest Mathieu function (pendular ground state)

$$\psi^{(0)}(\theta, t=0) = \phi_0(\theta) = \frac{1}{\sqrt{\pi}}\mathrm{ce}_0\left(\frac{\theta}{2}; 2V\right) \tag{17}$$

The resulting wave packet can be written in terms of eigen energies $\tilde{E}$ and eigenfunctions $\tilde{u}$ of the "new" Hamiltonian with changed barrier height $\tilde{V}$

$$\psi^{(0)}(\theta, t) = \sum_{n=0}^{\infty} c_{2n}^{(0)} \exp\left(-i\tilde{E}_{2n}t\right)\tilde{\phi}_{2n}(\theta) \tag{18}$$

The corresponding expansion coefficients $c_{2n}^{(0)}$ of the "old" wave function in the basis of the "new" ones are most conveniently calculated using the Fourier representation introduced in (6,7)

$$\begin{aligned} c_{2n}^{(0)} &\equiv \int_0^{2\pi} \phi_0(\theta)\tilde{\phi}_{2n}(\theta)\, d\theta \\ &= A_0^{(0)}\tilde{A}_0^{(2n)} + \sum_{k=0}^{\infty} A_k^{(0)}\tilde{A}_k^{(2n)} \end{aligned} \tag{19}$$

where $\tilde{A}$ are the Fourier coefficients of the solutions $\tilde{\phi}$ of the Mathieu equation (2) but with $\tilde{V}$ or $\tilde{q}$, which are again obtained with the matrix-based method described above. Note that for the special case of $V = \tilde{V}$ the orthonormality of the eigenfunctions results in $c_{2n}^{(0)} = \delta_{n,0}$.

In principle, the dynamics of the squeezed state analogue is completely determined by (18) together with coefficients (19). Throughout the remainder of this work we assume an initial barrier height of $V = 100$ with the corresponding ground pendular energy level $E_0 = 3.5$ lying far below the potential barrier. The probability densities, $|\psi(\theta, t)|^2$, associated with the squeezed wave packets are shown in Fig. 2. For $\tilde{V} = 10$ the density is centered around the potential energy minimum at $\theta = \pi$ with its width oscillating in a nearly periodic manner. More complicated patterns are observed for $\tilde{V} = 1$ and for $\tilde{V} = 0$ where the wave functions are able to cross the barrier. The corresponding probability distributions are found to span the whole range $[0, 2\pi]$ of the periodic coordinate θ giving rise to complicated interference patterns. Of particular interest is the barrier-less case, $\tilde{V} = 0$, where revival phenomena are observed, *vide infra*

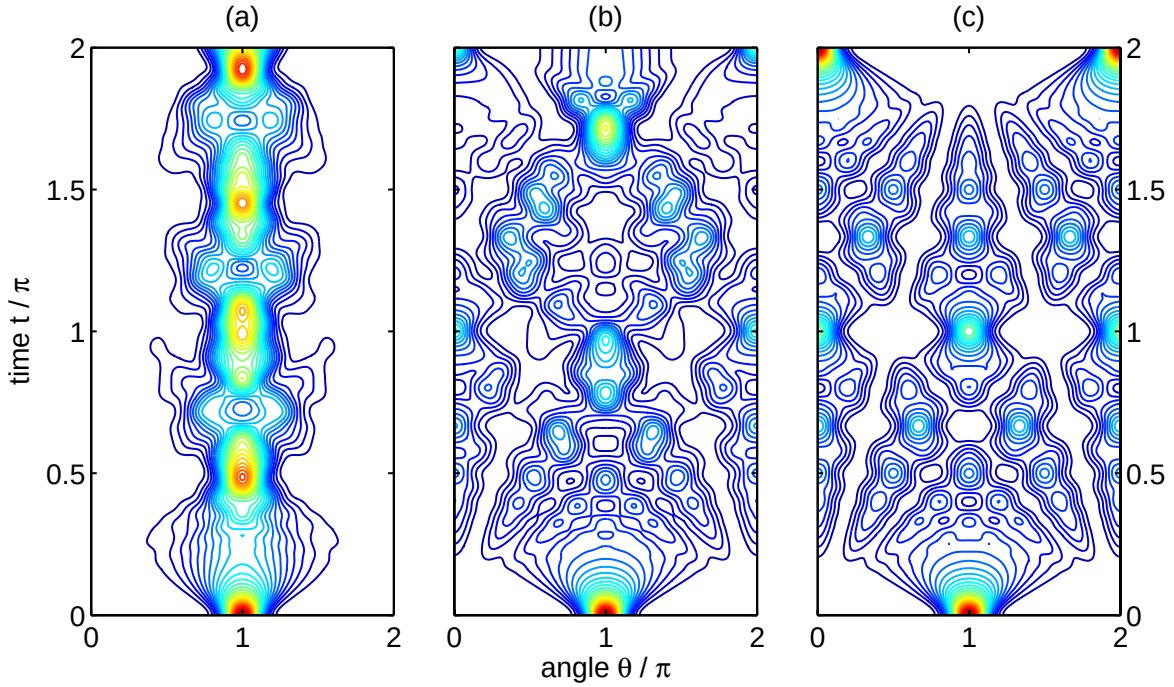

FIG. 2: Probability densities $|\psi(\theta,t)|^2$ for squeezed pendular states with $\tilde{V}=10$ (a), $\tilde{V}=1$ (b), $\tilde{V}=0$ (c). In all cases, $V=100$.

The knowledge of the time-dependent densities allows us to calculate expectation values of arbitrary observables of interest. The most important one is again the mean orientation for which time–independent results were already discussed above

$$\begin{aligned}\langle\cos\theta\rangle^{(0)}(t) &= \int_0^{2\pi}|\psi(\theta,t)|^2\cos\theta\,d\theta \\ &= \sum_{n,n'=0}^{\infty} c_{2n}^{(0)}c_{2n'}^{(0)}\exp\left[-i(\tilde{E}_{2n}-\tilde{E}_{2n'})t\right]\langle\tilde{\phi}_{2n'}|\cos\theta|\tilde{\phi}_{2n}\rangle \qquad (20)\end{aligned}$$

Hence, the dynamical degree of orientation of squeezed pendular wave functions comprises of oscillatory summands whose frequencies reflect energy gaps in the spectrum of the "new" pendular states $\tilde{E}$, weighted with products of coefficients c and with matrix elements of the orientation cosine for the "new" potential barrier $\tilde{V}$.

Time dependent mean orientations are shown in the left panel of Fig. 3 for different values of $\tilde{V}=10,1,0$ and for an identical value $V=100$. They display an oscillatory behavior reflecting the Bohr frequencies associated with the populated states. These can be identified from the corresponding energy distributions $|c_{2n}^{(0)}|^2$ shown in the right panel of

Fig. 3. They show that upon a sudden decrease of the potential barrier height, the wave packets mainly ($|c_{2n}^{(0)}|^2 > 0.1$) comprises of only two, three and four eigen states of the new potential, respectively.

In the following two paragraphs, we shall proceed in analogy to the discussion of stationary states of the plane quantum pendulum in the literature [7, 19], i. e., we consider the two limiting cases of the harmonic oscillator and of the free rotor. Sometimes we shall additionally replace the Fourier coefficients $A_k^{(0)}$ of the initial, pendular ground state by the harmonic approximation (12a,b) which is well–justified for $E_0 \ll V$ for our particular choice of the barrier height, $V = 100$. Together with the assumption of very large or very small values of the "new" barrier height $\tilde{V}$, this will simplify the expressions for eigen energies $\tilde{E}$, eigenfunctions $\tilde{u}$, and corresponding Fourier coefficients $\tilde{A}, \tilde{B}$ which allows us to derive analytical expressions from the above formula (20) for the time–dependence of the mean orientation.

It is noted that the transition from the oscillator to the rotor limit can also be considered as a transition from classical to quantum dynamics: While coherent states in a harmonic oscillator represent the closest quantum analogue to classical vibrational dynamics, the dynamics of rotor states is subject to pronounced quantum phenomena such as interference and wave packet revivals [26, 43], *vide infra*.

A. Harmonic oscillator limit

Let us first consider the case where the energies of all notably populated states, $|c_{2n}^{(0)}|^2 > \epsilon$, are well below the "new" potential barrier, $\tilde{E}_{2n} \ll \tilde{V}$. Hence, the corresponding Fourier coefficients $\tilde{A}^{(2n)}$ in (19) can be replaced by their harmonic approximation (12a,b). In this case, the quantum dynamics is identical to that of a squeezed state of a non–periodic harmonic oscillator [24, 25]. The evolving wave packet remains Gaussian shaped with its center at $\xi = 0$. Its width is periodic in time, where the widths in position and momentum representations oscillate out of phase. This behavior is approximately realized in Fig. 2 (a) for $\tilde{V} = 10$ which is rather close to the harmonic limit while for $\tilde{V} = 1$ notable deviations of the Gaussian shape occur already during the first period of vibration.

The corresponding expansion coefficients (19) are obtained as projections of the "old" wave function ϕ_0 onto the basis of the "new" oscillator eigenfunctions $\tilde{\phi}_{2n}$ with squeeze

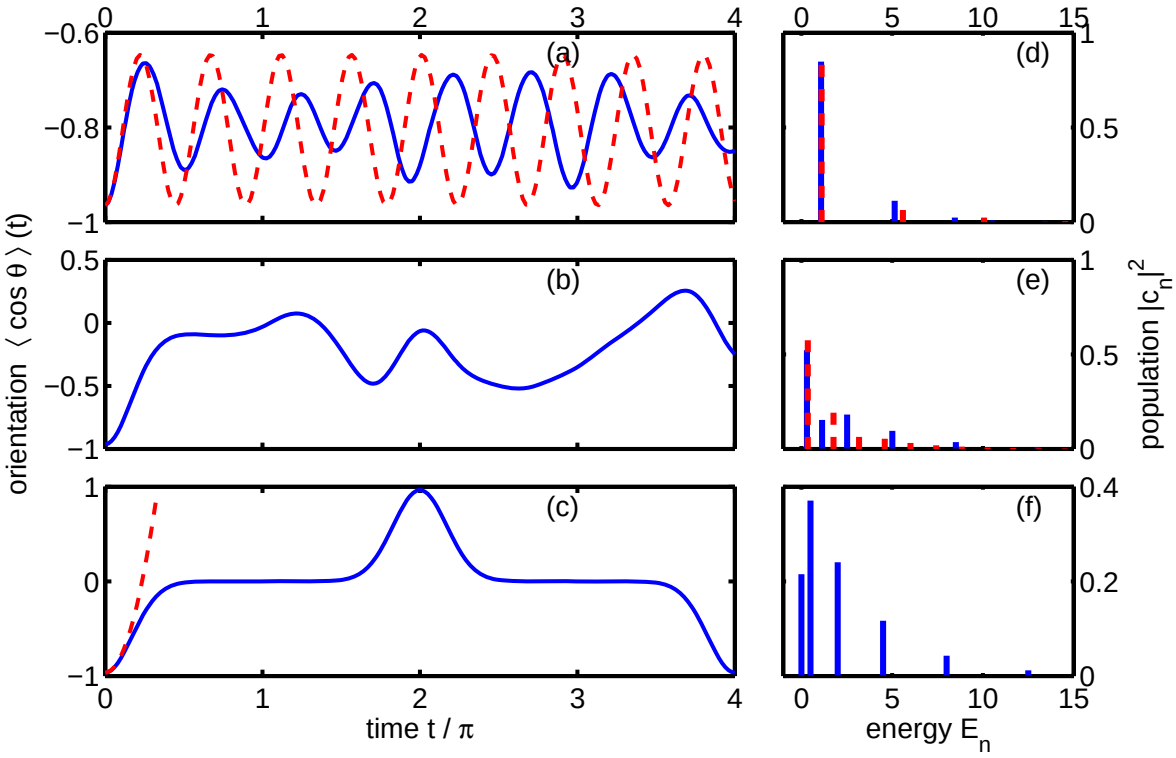

FIG. 3: Left: Mean orientation $\langle\cos\theta\rangle(t)$ for squeezed pendular states with (a) $\tilde{V} = 10$, (b) $\tilde{V} = 1$, (c) $\tilde{V} = 0$. Dashed (red) curve in (a) shows results for the squeezed state of the limiting harmonic oscillator (22) while dashed (red) curve in (c) is for free particle dynamics without periodic boundary conditions (30). Right: Corresponding energy distributions $|c_{2n}|^2$. Solid (blue) bars: Exact values. Dashed (red) bars: Harmonic approximation (21). In all cases, $V = 100$.

parameter $s = \sqrt{V/\tilde{V}}$, see Ref. [26]

$$c_{2n}^{(0)} = (-1)^n \left(\frac{2\sqrt{s}}{s+1}\right)^{1/2} \left(\frac{s-1}{s+1}\right)^n \frac{(2n-1)!!}{\sqrt{(2n)!}} \tag{21}$$

where the coefficients c_{2n+1} vanish due to the even symmetry of the initial state ϕ_0. These results are shown as dashed (red) bars in the right panel of Fig. 3. While they still represent a good approximation of the case of $\tilde{V} = 10$, major deviations occur for $\tilde{V} = 1$, see Fig. 3 (d,e).

In analogy to our treatment of the harmonic oscillator limit of stationary pendular states (13), the expectation value of the orientation can be approximated by a truncated Taylor expansion

$$\langle\cos\theta\rangle^{(0)}(t) \approx -1 + \frac{1}{2}\langle\xi^2\rangle^{(0)} = -1 + \frac{1}{2}\left[\delta\xi^{(0)}(t)\right]^2 + \frac{1}{2}\left[\langle\xi\rangle^{(0)}(t)\right]^2 \tag{22}$$

with $\langle\xi\rangle^{(0)}(t) = 0$ and with the well–known result for the time–dependent position uncertainty of a squeezed state [26]

$$\left[\delta\xi^{(0)}(t)\right]^2 = \frac{1}{2\tilde{\omega}}\left[s\sin^2(\tilde{\omega}t) + \frac{1}{s}\cos^2(\tilde{\omega}t)\right] \tag{23}$$

where $\tilde{\omega} = \sqrt{\tilde{V}/2}$ is the classical frequency of harmonic oscillation. For comparison, this result is illustrated for $\tilde{V} = 10$ as a dashed (red) curve in Fig. 3 (a). The numerically exact result oscillates slightly slower in time, and with less modulation, than the harmonic approximation resulting in a notable phase mismatch already after a few periods of vibration. A synopsis with the right panel of the figure reveals that this discrepancy is rather due to the energy levels $\tilde{E}_n$ than the corresponding populations $|c_{2n}^{(0)}|^2$.

B. Free rotor limit

Next, we consider the case when the energies of all notably populated states ($|c_{2n}|^2 > \epsilon$) are high above the "new" potential barrier, $\tilde{V} \ll \tilde{E}_{2n}$. The extreme case of $\tilde{V} \to 0$ corresponds to a sudden turn-off of the hindering potential, see also Ref. [21]. Note that similar situations could indeed be realized in molecular alignment experiments by adiabatic turn-on and sudden turn-off of the laser field [38, 39]. In that case, the corresponding wave packet is described by the free rotor approximation (16) for the "new" Fourier coefficients $\tilde{A}$. Then the expansion coefficients are simply obtained as

$$c_0^{(0)} = \sqrt{2}A_0^{(0)} \tag{24a}$$

$$c_{2n}^{(0)} = A_n^{(0)} \tag{24b}$$

with $n > 0$ and where the coefficients c_{2n+1} vanish again. Hence, expression (18) for the wave packet with free rotor energies $\tilde{E}_{2n}$ and eigenfunctions $\tilde{\phi}_{2n}$ yields

$$\psi^{(0)}(\theta, t) = \frac{1}{\sqrt{\pi}}\sum_{n=0}^{\infty} A_n^{(0)} \exp\left[-in^2\frac{t}{2}\right]\cos(n\theta). \tag{25}$$

The time evolution of the corresponding density is shown in Fig. 2(c). The initially very narrow Gaussian–like wave packet starts to spread. For $t/\pi \leq 0.1$, the behavior is essentially equal to the evolution of a free particle wave packet on an infinite domain [44]. At later times, however, the wave packet starts to interfere with itself through the periodic boundary

conditions giving rise to a plethora of interference phenomena. It can be seen from Eq. (25) that at the full revival time ($t/\pi = 4$, not shown in the figure) the wave packet has regained its initial, Gaussian bell shape, centered at $\theta = \pi$

$$\psi^{(0)}(\theta, 4\pi) = \psi^{(0)}(\theta, 0). \tag{26}$$

At the half revival time $t/\pi = 2$, the wave packet is again Gaussian–shaped but shifted by π yielding [43]

$$\psi^{(0)}(\theta, 2\pi) = \psi^{(0)}(\theta - \pi, 0) \tag{27}$$

because the phase factors in Eq. (25) are real–valued for $t/\pi = 4$ and $t/\pi = 2$ with equal or alternating signs, respectively. For the quarter revival time, $t/\pi = 1$, a superposition of the above wave functions is obtained [43]

$$\psi^{(0)}(\theta, \pi) = \frac{1}{\sqrt{2}} \left[e^{-i\frac{\pi}{4}} \psi^{(0)}(\theta, 0) + e^{+i\frac{\pi}{4}} \psi^{(0)}(\theta, 2\pi) \right] \tag{28}$$

because the phase factors in Eq. (25) are 1 and $-i$ for even and odd n, respectively. Similar fractional revivals with a splitting of the wave packet in three, four, etc., lobes are partly visible in Fig. 2(c) for $t/\pi = 2/3, 1/2$, etc.

In addition to the purely temporal patterns observed at the (fractional) revival times, the space-time representation of the evolving probability density in the free rotor limit exhibits further structure, similar to the "quantum carpets" previously found for, e. g., a particle in a square well [34]. In particular, our Fig. 2(c) shows an intriguing combination of spatial and temporal structures: In between linear canals around $\theta = \pm t/2, \pm 3t/2, \pm 5t/2, \ldots$, where the density practically vanishes, there are linear ridges at $\theta = 0, \pm t, \pm 2t, \ldots$, where the density exhibits maxima, interspersed by saddles. Another set of such ridges can be seen at $\theta = \kappa t/2 + \pi$ for integer κ but without interlacing canals. All of these patterns become more and more washed out for increasing orders, i. e., for higher values of the slopes of the characteristic $\theta(t)$ rays. The point where the canals and ridges finally become invisible moves to higher orders for decreasing width of the initial wave packet. In the context of squeezed pendular states, this can be realized by increasing the barrier height V of the original trigonometric potential in Eq. (1). For an in-depth analysis of these space-time structures, the reader is referred to App. A.

Equation (25) also allows for a ready evaluation of expectation values of observables of interest. Again, we consider the orientation cosine as the most important quantity in the

characterization of pendular states with $m = 1$. Inserting the expansion coefficients (24) and the energy levels for the free rotor limit (15) into Eq. (20) one obtains

$$\begin{aligned}\langle\cos\theta\rangle^{(0)}(t) &= \frac{1}{\pi}\sum_{n,n'=0}^{\infty} A_n^{(0)} A_{n'}^{(0)} \exp\left[-i(n^2-n'^2)\frac{t}{2}\right]\int_0^{2\pi}\cos(n'\theta)\cos\theta\cos(n\theta)\,d\theta \\ &= A_0^{(0)}A_1^{(0)}\cos\left(\frac{t}{2}\right) + \sum_{n=0}^{\infty} A_n^{(0)}A_{n+1}^{(0)}\cos\left[(2n+1)\frac{t}{2}\right] \end{aligned} \tag{29}$$

The time dependence of the mean orientation is shown in Fig. 3 (c) and can be readily understood in connection with Fig. 2 (c): The initial spread of the wave packet is reflected by a rapid loss of orientation. Up to $t/\pi \lesssim 0.1$, the result is similar to the dispersion of a free particle Gaussian wave packet without periodic boundary conditions [44]

$$\langle\cos\theta\rangle^{(0)}(t) = -1 + \frac{1}{4\omega}\left[1+(\omega t)^2\right] \tag{30}$$

which can be easily derived from Eq. (22), see also the dashed curve in Fig. 3 (c). At the half revival time, $t/\pi = 2$, the shifted Gaussian centered at $\theta = 0$ leads to strong anti–orientation, $\langle\cos\theta\rangle \approx 1$. In between those two times, the mean orientation practically vanishes, and at the quarter revival time, $t/\pi = 1$, the double Gaussian structure leads exactly to $\langle\cos\theta\rangle^{(0)} = 0$.

Next, we insert the harmonic approximation (12) for the Fourier coefficients of the ground vibrational state $A_k^{(0)}$ into Eq. (29), which is well justified for the rather large value of $V = 100$ considered here. As will be shown in App. B, the mean orientation can be expressed in terms of a Mathieu sine elliptic function in time

$$\langle\cos\theta\rangle^{(0)}(t) = \left(\frac{2}{\pi\beta^2}\right)^{1/4}\exp\left(-\frac{1}{4\beta^2}\right)\mathrm{se}_1\left(\frac{t-\pi}{2};\frac{V}{2}\right) \tag{31}$$

where the harmonic oscillator limit of Mathieu functions (12) was used again. The pre-factor of the sine elliptic function rapidly approaches unity for increasing barrier height. For the value $V = 100$ used here we find $-\langle\cos\theta\rangle^{(0)}(0) = \langle\cos\theta\rangle^{(0)}(2\pi) \approx 0.9586$

IV. PENDULAR ANALOGUE OF COHERENT STATES

In this section, the generalization of a coherent state to a periodic situation with a trigonometric potential is discussed. In analogy to coherent states of a harmonic oscillator, we shall consider a situation where the trigonometric potential in (1) is shifted horizontally

by $\bar{\theta}$ but the barrier height ($V = \bar{V}$) as well as the eigen energies ($E = \bar{E}$) remain unchanged. The resulting eigenfunctions of the "new" potential are given by shifting the Fourier series (6)

$$\bar{\phi}_{2n}(\theta) \;=\; \frac{1}{\sqrt{\pi}} \sum_{k=0}^{\infty} A_k^{(2n)} \cos[k(\theta - \bar{\theta})] \tag{32a}$$

$$\bar{\phi}_{2n+1}(\theta) \;=\; \frac{1}{\sqrt{\pi}} \sum_{k=1}^{\infty} B_k^{(2n+1)} \sin[k(\theta - \bar{\theta})] \tag{32b}$$

In analogy to Eq. (18), pendular analogues of coherent state wave packets can be expressed in terms of the above wave functions

$$\begin{aligned} \psi^{(0)}(\theta, t) \;&=\; \sum_{n=0}^{\infty} c_{2n}^{(0)} \exp\left(-iE_{2n}t\right) \bar{\phi}_{2n}(\theta) \\ &+\; \sum_{n=0}^{\infty} c_{2n+1}^{(0)} \exp\left(-iE_{2n+1}t\right) \bar{\phi}_{2n+1}(\theta) \end{aligned} \tag{33}$$

where the eigen energies (3) are unchanged. Note that in the most general case ($\pi \neq \bar{\theta} \neq 0$) the shifted basis functions are neither even nor odd with respect to inversion at $\theta = 0$. Hence, the even initial wave function, which is again taken as the lowest eigen state of the Mathieu equation (17) for the unchanged potential, has non–vanishing overlap with both even– and odd–numbered eigenfunctions of the shifted potential

$$c_{2n}^{(0)} \;=\; \int_0^{2\pi} \phi_0(\theta) \bar{\phi}_{2n}(\theta)\, d\theta = A_0^{(0)} A_0^{(2n)} + \sum_{k=0}^{\infty} A_k^{(0)} A_k^{(2n)} \cos(k\bar{\theta}) \tag{34a}$$

$$c_{2n+1}^{(0)} \;=\; \int_0^{2\pi} \phi_0(\theta) \bar{\phi}_{2n+1}(\theta)\, d\theta = -\sum_{k=1}^{\infty} A_k^{(0)} B_k^{(2n+1)} \sin(k\bar{\theta}) \tag{34b}$$

which converges for $\bar{\theta} \to 0$ to the squeezed state result (19) but for the special case $V = \tilde{V}$ with $c_{2n}^{(0)} = \delta_{n,0}$ due to the orthonormality of the underlying trigonometric functions.

Ansatz (33) for the wave function together with coefficients (34) fully determines the wave packet dynamics. Corresponding probability distributions are shown in Fig. 4. While for $\bar{\theta} = \pi/8$ the distributions are essentially centered along the classical trajectory, the densities become more blurred for $\bar{\theta} = \pi/2$ after few periods of vibration. Finally, for $\bar{\theta} = \pi$, the wave packet is subject to strong interference phenomena resulting from the boundary conditions. This knowledge of the time-dependent probabilities can be used in principle to calculate expectation values of any observable of interest, such as the mean orientation displayed in

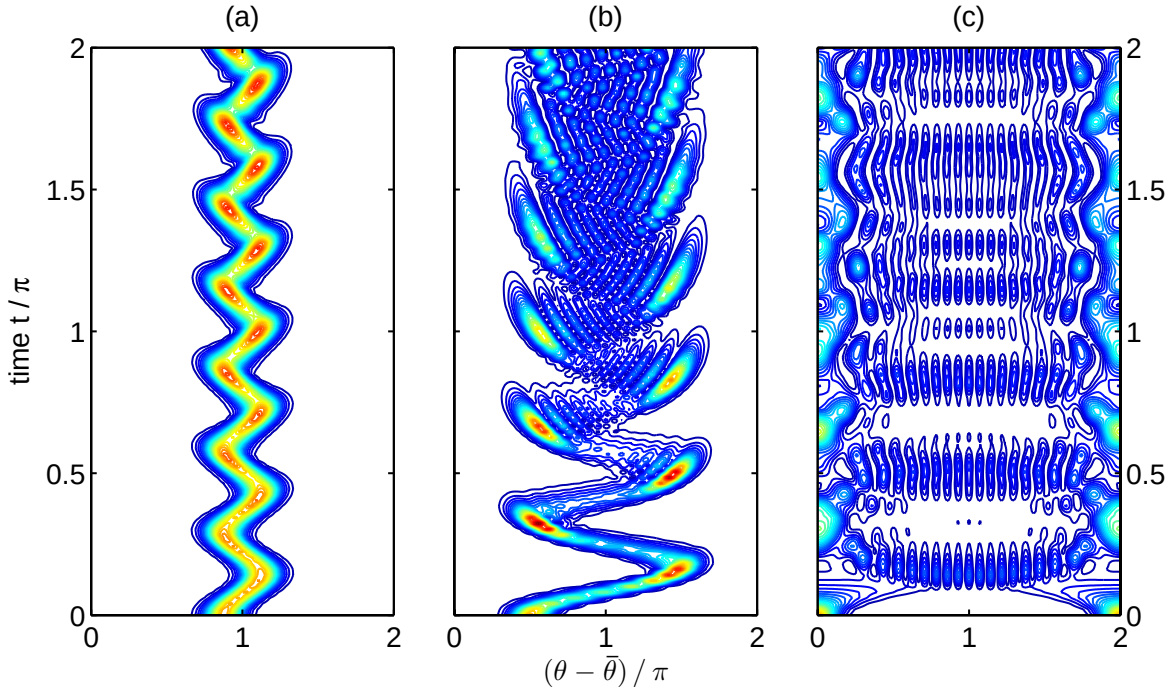

FIG. 4: Probability densities $|\psi(\theta,t)|^2$ for coherent pendular states with $\bar{\theta}=\pi/8$ (a), $\bar{\theta}=\pi/2$ (b), $\bar{\theta}=\pi$ (c). In all cases, $V=100$.

the left panel of Fig. 5. In analogy to the squeezed pendular state (20), the result for the coherent pendular state is given by

$$\langle\cos\theta\rangle^{(0)}(t)=\sum_{n,n'=0}^{\infty}c_n^{(0)}c_{n'}^{(0)}\exp\left[-i(E_n-E_{n'})t\right]\langle\bar{\phi}_{n'}|\cos\theta|\bar{\phi}_n\rangle \tag{35}$$

where the index extends over both even and odd states. Again, the orientational dynamics is governed by the energy gaps of the pendular spectrum together with the probability amplitudes c_n shown in the right panel of Fig. 5. In the following, we shall investigate two special cases in more detail, i. e., that of small ($\bar{\theta}\ll\pi$) and of largest possible ($\bar{\theta}=\pi$) displacement leading to potential inversion.

A. Limit of small displacements (harmonic limit)

First, we consider the limit of small displacements, $\bar{\theta}\ll\pi$. Because the energies of the pendular ground state both before and after the sudden shift of the potential are well below the barrier, all Fourier coefficients A, B can be replaced by their harmonic counterparts

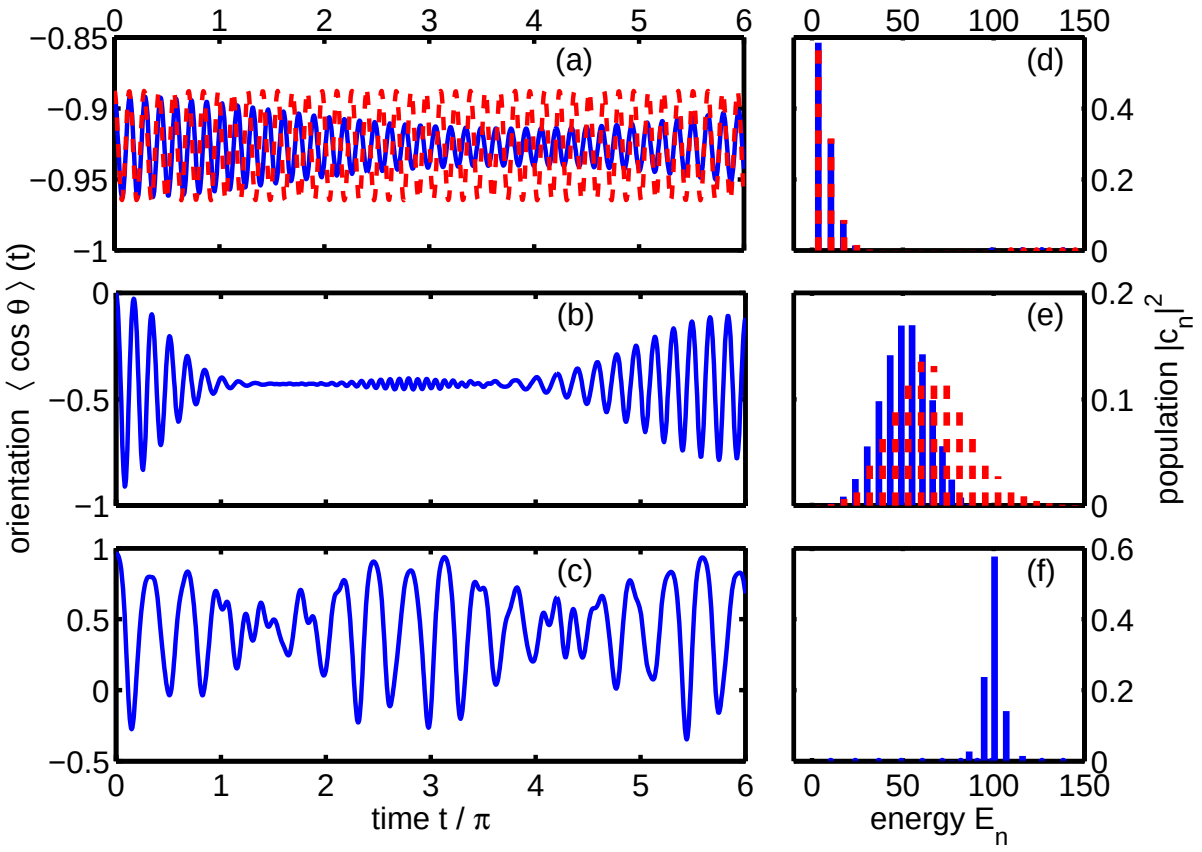

FIG. 5: Left: Mean orientation $\langle\cos\theta\rangle(t)$ for coherent pendular states with $\bar{\theta} = \pi/8$ (a), $\bar{\theta} = \pi/2$ (b), $\bar{\theta} = \pi$ (c). Dashed (red) curve in (a) shows results for the squeezed state of the limiting harmonic oscillator. Right: Corresponding energy distributions $|c_n|^2$. Solid (blue) bars: Exact values. Dashed (red) bars: Harmonic approximation (36). In all cases, $V = 100$.

(12). In that case, the situation approaches a coherent state of a (non–periodic) harmonic oscillator: Because the potential minimum does not coincide with the center of the Gaussian packet any more, the latter starts to move along the classical trajectory with its shape and width unchanged which resembles a classical harmonic oscillator most closely [24, 25]. Such a situation is approximately realized in our simulations for $\bar{\theta} = \pi/8$ for which the time–dependence of the mean orientation cosine is shown in Fig. 5(a). For comparison the coherent state result is shown as a dashed (red) curve. It is obtained from Eq. (22) with the trajectory $\langle\xi\rangle^{(0)}(t) = \bar{\theta}\cos(\omega t)$ and with constant width $\left[\delta\xi^{(0)}(t)\right]^2 = 1/(2\omega)$ which is derived from Eq. (23) with $s = 1$.

The well–known expansion coefficients of a coherent state in a non–periodic domain are

given by [26]

$$c_n^{(0)} = \frac{\alpha^n}{\sqrt{n!}} \exp\left(-\frac{\alpha^2}{2}\right) \tag{36}$$

with $\alpha = \bar{\theta}\beta/\sqrt{2}$. The corresponding energy distribution, $|c_n^{(0)}|^2$, is a Poisson distribution in α^2. Fig. 5(d) shows that for the wave packet state with $\bar{\theta} = \pi/8$, where only the lowest three eigen states bear notable population, the energy levels and populations are practically indistinguishable from the corresponding harmonic results. Nevertheless, the tiny anharmonicity gives rise to the slow modulation of the amplitudes of $\langle\cos\theta\rangle^{(0)}(t)$ seen in Fig. 5(a). More pronounced deviations from the harmonic results occur for $\bar{\theta} = \pi/2$, where nine states are essentially populated with a peak around $E_n \approx 50$, see Fig. 5(e). These discrepancies clearly show up in the dynamics of the orientation cosine shown in Fig. 5(b) where the amplitudes of the vibrations are subject to strong interference phenomena which can be explained in the context of revival theory [43]. In passing it is noted that more general results for coherent states of a harmonic oscillator are given, e. g., in Ref. [26] for a combined change of the barrier height ($s \neq 1$) and shift of the minimum position ($\alpha \neq 0$) which shall not be considered here for reasons of brevity.

B. Limit of largest displacement (potential inversion)

In the paragraph above, we considered the case where $\bar{\theta} \ll \pi$ was so small that both the initial (ϕ_0) and the final ($\bar{\phi}_n$) wave functions could be described within the harmonic approximation. However, when going to larger displacements $\bar{\theta}$, higher and higher pendular states become initially populated and the harmonic approximation is no longer valid. In the extreme case of the largest possible displacement, $\bar{\theta} = \pi$, an inversion of the trigonometric potential energy, i. e., a sudden exchange of minima and maxima of the potential energy curve occurs which is equivalent to a squeezed state with $\tilde{V} = -V$. This setting is also referred to as inverted pendulum. For a comparison of classical, semiclassical and quantum-mechanical results for the fall times of an inverted pendulum, see Ref. [20]. In the realm of molecules, qualitatively similar situations are realized in photoinduced dynamics of intramolecular torsional degrees of freedom: Upon excitation of suitable electronic states, the positions of minima and maxima may be swapped [36, 45, 46]. A typical example is the photo-induced torsion around a CC or CN double bond, where a potential inversion occurs between the electronic ground state and and excited electronic state, see [47] and references

therein)

Due to the special symmetry of the inverted potential for $\bar{\theta} = \pi$, it is evident from Eq. (34) that the initial wave packet comprises of even–numbered (cosine elliptic) eigen states of the potential only. Fig. 5(f) shows that for the case of $V = 100$ considered here, only three states with $n = 16, 18, 20$ close to the barrier of the trigonometric potential essentially contribute to the wave packet. These states are found at energies of $E_{16} \approx 94.9$, $E_{18} \approx 100.6$, and $E_{20} \approx 107.0$. The corresponding probability densities are centered near the maxima of the potential energy function thus resulting in anti–orientation as shown in Fig. 1. The low number of contributing states alleviates an interpretation of the timescales observed in the time–dependence of the orientation cosine shown in Fig. 5(e). Based on Eq. (35), the mean orientation displays oscillatory behavior with the Bohr frequencies corresponding to the energy gaps between those states. There are three vibrational periods observed: The period of the carrier frequency is approximately $\pi/3$, its amplitude being modulated with a period of about 3π. Occasionally, a frequency doubling of the carrier is seen, e. g. around $\pi \leq t \leq 3\pi/2$. Indeed, it is straightforward to assign these periods to the energy gaps $E_{20} - E_{18} \approx 6.4$ or $E_{18} - E_{16} \approx 5.7$, $E_{20} + E_{16} - 2E_{18} \approx 0.7$, and $E_{20} - E_{16} \approx 12.1$, respectively.

V. PENDULAR ANALOGUE OF DOUBLE WELL POTENTIAL

In this section we shall turn our attention to a double well pendulum as defined in Eq. (1) with $m = 2$. The corresponding potential energy curve displays two minima at $\theta = \pi/2, 3\pi/2$ separated by barriers of height V at $\theta = 0, \pi$. In analogy to our discussion of stationary states of the single well potential ($m = 1$), the quantum–mechanical eigen states of the double well potential can be expressed in terms of Mathieu's cosine elliptic (ce) or sine elliptic (se) functions [15–17]. Inserting the multiplicity $m = 2$ into Eq. (5) immediately yields (with $\eta = \theta$ and $q = V/2$)

$$\phi_{2n}(\theta) = \frac{1}{\sqrt{\pi}} \mathrm{ce}_n\left(\theta; \frac{V}{2}\right) \tag{37a}$$

$$\phi_{2n+1}(\theta) = \frac{1}{\sqrt{\pi}} \mathrm{se}_{n+1}\left(\theta; \frac{V}{2}\right) \tag{37b}$$

These wave functions can be categorized with respect to two different symmetry properties [17]. The first one is the symmetry with respect to reflection at the potential minima at

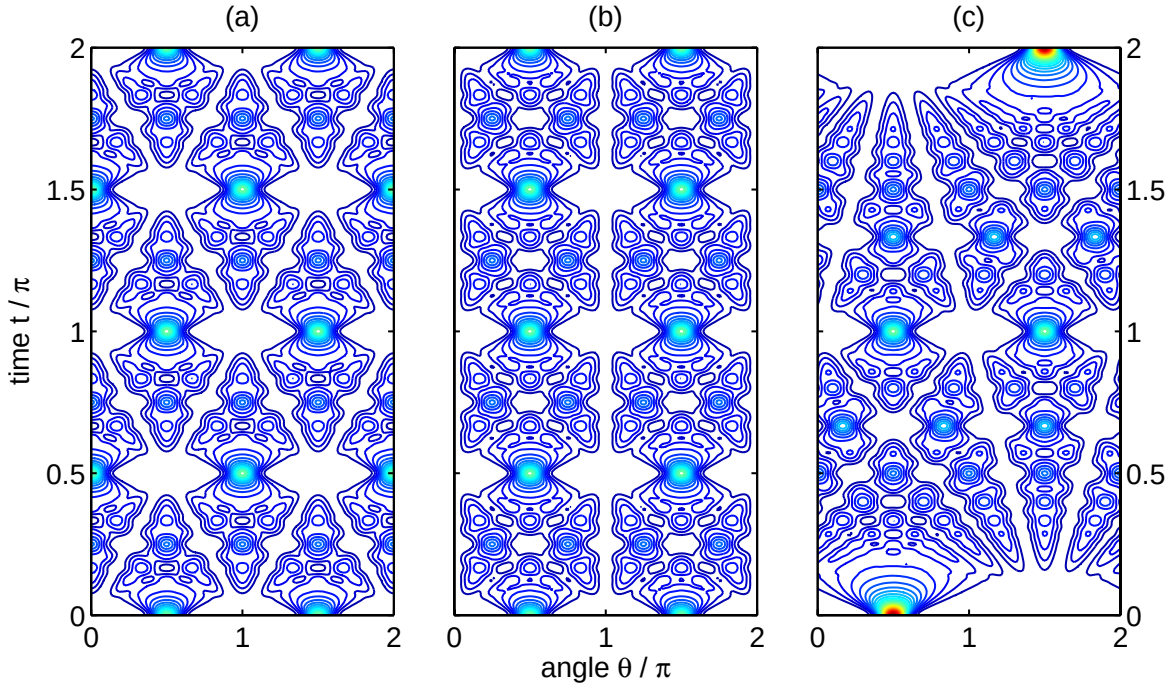

FIG. 6: Probability densities $|\psi(\theta,t)|^2$ for squeezed pendular states of a double well potential ($V = 100$) in the free rotor limit ($\tilde{V} = 0$). Even (a), odd (b), and localized (c) initial states.

$\theta = \pi/2, 3\pi/2$ which is equivalent to the even/odd symmetry of the wave functions of the single well potential. Note that for the double well situation ce–functions of even order and se–functions of odd order are even at the potential minima. In addition, the states of the double well potential can be of g (*gerade*, even) or u (*ungerade*, odd) symmetry with respect to inversion at the potential barrier at $\theta = \pi$ which manifests itself in the difference between ce(g) and se(u) functions. This symmetry, throughout the remainder of this article referred to as parity, gives rise to a class of genuine phenomena in quantum dynamics of the double well pendulum, ranging from tunneling to interference and revival phenomena, as discussed in the following subsections on the harmonic oscillator limit and on the free rotor limit, respectively. To this end, we shall restrict ourselves to the consideration of the ground state doublet (even symmetry with respect to reflection at potential minima) which

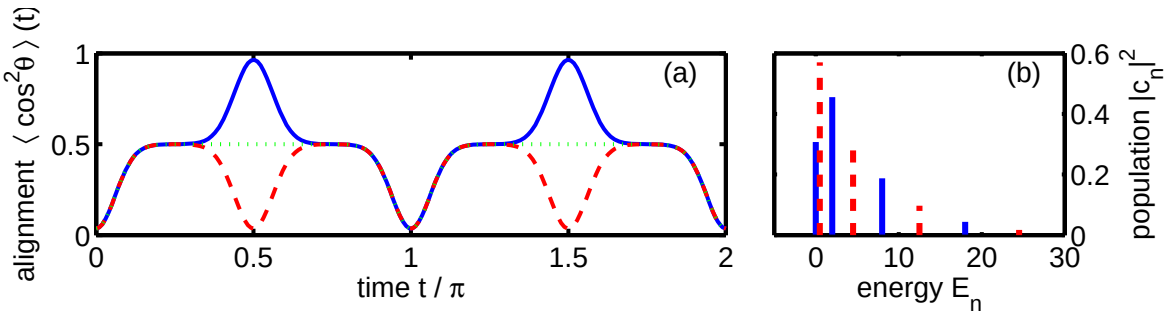

FIG. 7: Left: Mean alignment $\langle\cos^2\theta\rangle(t)$ for squeezed pendular states of a double well potential ($V = 100$) in the free rotor limit ($\tilde{V} = 0$). Even (solid blue curve), odd (dashed red curve), and localized (dotted green curve) initial states. Right: Corresponding energy distributions $|c_n|^2$. Solid (blue) bars: Even wave function. Dashed (red) bars: Odd wave function.

can be expressed by the following two Fourier series

$$\phi^{(g)}(\theta) = \frac{1}{\sqrt{\pi}}\mathrm{ce}_0\left(\theta;\frac{V}{2}\right) = \frac{1}{\sqrt{\pi}}\sum_{k=0}^{\infty} A_k^{(g)}\cos[2k\theta] \tag{38a}$$

$$\phi^{(u)}(\theta) = \frac{1}{\sqrt{\pi}}\mathrm{se}_1\left(\theta;\frac{V}{2}\right) = \frac{1}{\sqrt{\pi}}\sum_{k=0}^{\infty} B_k^{(u)}\sin[(2k+1)\theta] \tag{38b}$$

where the absence of odd or even order Fourier coefficients reflects the g or u parity, respectively. For the barrier height $V = 100$ chosen for all calculations presented in this article, this pair of states is quasi–degenerate with a tunnel splitting $\Delta E = E^{(u)} - E^{(g)} \approx 1.2\times10^{-10}$.

A. Harmonic oscillator limit

When the energies of pendular states are well below the barrier height ($E_n \ll V$), the harmonic approximation for the Hamiltonian (1) for $m = 2$ can be invoked in the vicinity of the minima of the trigonometric potential energy function

$$\hat{H}_{1,2} = -\frac{1}{2}\frac{d^2}{d\xi_{1,2}^2} + V\xi_{1,2}^2 \tag{39}$$

for small values of the displacement coordinates $\xi_1 = \theta - \pi/2$ and $\xi_2 = \theta - 3\pi/2$. This is similar to the harmonic approximation (9) for the single well pendulum but with a four times higher force constant. Hence, the corresponding eigenfunctions of g and u parity can be approximated by linear combinations of Gaussian packets located at $\theta = \pi/2$ and at

$\theta = 3\pi/2$

$$\phi^{(g)}(\theta) = \frac{1}{\sqrt{2}} N_0 \left[\exp\left(-\beta^2(\theta - \pi/2)^2/2\right) + \exp\left(-\beta^2(\theta - 3\pi/2)^2/2\right) \right] \tag{40a}$$

$$\phi^{(u)}(\theta) = \frac{1}{\sqrt{2}} N_0 \left[\exp\left(-\beta^2(\theta - \pi/2)^2/2\right) - \exp\left(-\beta^2(\theta - 3\pi/2)^2/2\right) \right] \tag{40b}$$

with $\beta \equiv (2V)^{1/4}$. In the context of pendular dynamics, these wave functions have to be adapted to periodic boundary conditions by expressing them in terms of the Fourier series (38) with coefficients (for $k > 0$)

$$A_0^{(g)} = \frac{N_0}{\beta} \tag{41a}$$

$$A_k^{(g)} = 2\frac{N_0}{\beta}(-1)^k \exp\left[-\frac{(2k)^2}{2\beta^2}\right] \tag{41b}$$

$$B_k^{(u)} = 2\frac{N_0}{\beta}(-1)^k \exp\left[-\frac{(2k+1)^2}{2\beta^2}\right] \tag{41c}$$

Apart from a tiny tunnel splitting of the corresponding energy levels, there is no notable effect of parity, as long as the barrier is high enough to prevent interaction between the wave packets in the two wells. Hence, all of the results obtained for the harmonic oscillator limits of the squeezed and coherent pendular state analogues can be directly transferred from the single well to the double well potential. For example, the wave packet dynamics confined to the region of the single potential well displayed in Fig. 2 (a) and Fig. 4 (a,b) is essentially equivalent upon changing from $m = 1$ to $m = 2$, the only exception being the change in the force constant, $V/2 \to 2V$, (and corresponding changes $\beta \to \sqrt{2}\beta$ and $N_0 \to \sqrt[4]{2}N_0$) of the harmonic approximation to the trigonometric potentials, see Eq. (4). In particular, the phase difference between the g and u parity superposition states is not affecting any of the expectation values if wave functions are confined to the harmonic regimes of the potential.

B. Free rotor limit

The free rotor limit of a pendulum is approached if all considered energies vastly exceed the barrier height, $E_n \gg V$. In the double well case ($m = 2$), the eigenvalues and

eigenvectors of a free particle on a ring are written as

$$E_0^{(g)} = 0, \qquad \phi_0^{(g)}(\theta) = \frac{1}{\sqrt{2\pi}} \tag{42a}$$

$$E_{2n}^{(g)} = \frac{(2n)^2}{2}, \qquad \phi_{2n}^{(g)}(\theta) = \frac{1}{\sqrt{\pi}} \cos[2n\theta], \quad n > 0 \tag{42b}$$

$$E_{2n+1}^{(u)} = \frac{(2n+1)^2}{2}, \qquad \phi_{2n+1}^{(u)}(\theta) = \frac{1}{\sqrt{\pi}} \sin[(2n+1)\theta], \quad n \geq 0 \tag{42c}$$

Note that here only those subsets of the functions (15) are given, that are compatible with even symmetry at the potential minima and with the even (g) and odd (u) parity at the potential maximum.

As in our discussion of the free rotor limit of squeezed states for a single well pendulum, we now consider the pendular ground state doublet (38), subject to an instantaneous change of the potential barrier height, $\tilde{V} \to 0$. Setting the barrier height of the double well potential to zero, and choosing the g and u component of the quasi–degenerate ground state doublet as initial states, creates time-dependent wave packets which, in analogy to Eq. (18), can be expressed in terms of the free rotor eigen energies $\tilde{E}$ and eigenfunctions $\tilde{\phi}$ given above

$$\psi^{(g)}(\theta, t) = \sum_{n=0}^{\infty} c_{2n}^{(g)} \exp\left(-i\tilde{E}_{2n}^{(g)} t\right) \tilde{\phi}_{2n}^{(g)}(\theta) \tag{43a}$$

$$\psi^{(u)}(\theta, t) = \sum_{n=0}^{\infty} c_{2n+1}^{(u)} \exp\left(-i\tilde{E}_{2n+1}^{(u)} t\right) \tilde{\phi}_{2n+1}^{(u)}(\theta) \tag{43b}$$

$$\psi^{(l)}(\theta, t) = \frac{1}{\sqrt{2}} \left[\psi^{(g)}(\theta, t) + \psi^{(l)}(\theta, t)\right] \tag{43c}$$

where the third equation describes a localized wave function as a linear combination of g and u packets. Inserting the expansion coefficients for the free rotor limit

$$c_0^{(g)} = \sqrt{2} A_0^{(g)} \tag{44a}$$

$$c_{2n}^{(g)} = A_n^{(g)} \tag{44b}$$

$$c_{2n+1}^{(u)} = B_n^{(u)} \tag{44c}$$

with $n > 0$, which is the double well analog of Eq. (24), the wave packets are obtained as

$$\psi^{(g)}(\theta, t) = \frac{1}{\sqrt{\pi}} \sum_{n=0}^{\infty} A_n^{(g)} \exp\left[-i(2n)^2 \frac{t}{2}\right] \cos[2n\theta] \tag{45a}$$

$$\psi^{(u)}(\theta, t) = \frac{1}{\sqrt{\pi}} \sum_{n=0}^{\infty} B_n^{(u)} \exp\left[-i(2n+1)^2 \frac{t}{2}\right] \sin[(2n+1)\theta] \tag{45b}$$

It is noted that the first of the these equations is in complete analogy with Eq. (25). However, the restriction to even numbered indices is equivalent to the introduction of a scaled angle ($\theta \rightarrow 2\theta$) and a scaled time ($t \rightarrow 4t$), as predicted by Eq. (4).

The time evolutions of the corresponding g, u, l densities are displayed in Fig. 6. At earliest times, $t/\pi < 0.05$, the wave packets start to spread like those of a free particle, essentially identical for the three cases considered here. Due to the higher initial confinement of the Gaussian packets, this spread is much faster than in the case of the single well potential, see Eq. (30). At later times, the wave packets start to interfere with themselves, and a rich pattern of revival phenomena starts to develop. It is apparent from Eq. (45) that the first full revivals of the g, u and l wave packets are found at different times

$$\psi^{(g)}(\theta, \pi) = \psi^{(g)}(\theta, 0) \tag{46a}$$

$$\psi^{(u)}(\theta, 4\pi) = \psi^{(u)}(\theta, 0) \tag{46b}$$

$$\psi^{(l)}(\theta, 4\pi) = \psi^{(l)}(\theta, 0) \tag{46c}$$

which is a direct consequence of the (even/odd/none) parity of the initial wave functions. Also the appearance of the wave functions at the half revival time is qualitatively different

$$\psi^{(g)}(\theta, \pi/2) = \psi^{(g)}(\theta - \pi/2, 0) \tag{47a}$$

$$\psi^{(u)}(\theta, 2\pi) = -\psi^{(u)}(\theta, 0) \tag{47b}$$

$$\psi^{(l)}(\theta, 2\pi) = \psi^{(l)}(\theta - \pi, 0) \tag{47c}$$

i. e., while the even parity (g) wave function is shifted in angle by $\pi/2$, the odd (u) wave function only changes its sign. In contrast, a wave function initially localized in the left potential minimum ($\theta = 3\pi/2$) is found at the half revival time in the right minimum ($\theta = 3\pi/2$). At the quarter revival time, the g and l wave function split into two lobes separated by $\pi/2$ and π, respectively, whereas the u wave function merely acquires an overall phase factor

$$\psi^{(g)}(\theta, \pi/4) = \frac{1}{\sqrt{2}} \left[e^{-i\pi/4} \psi^{(g)}(\theta, 0) + e^{i\pi/4} \psi^{(g)}(\theta, \pi/2) \right] \tag{48a}$$

$$\psi^{(u)}(\theta, \pi) = -i\psi^{(u)}(\theta, 0) \tag{48b}$$

$$\psi^{(l)}(\theta, \pi) = \frac{1}{\sqrt{2}} \left[e^{-i\pi/4} \psi^{(l)}(\theta, 0) + e^{i\pi/4} \psi^{(l)}(\theta, 2\pi) \right] \tag{48c}$$

Furthermore, neither a doubling nor a shift of the spatial structures is observed for the odd

parity (u) case at the 1/8 revival time

$$\psi^{(u)}(\theta, \pi/2) = e^{-i\pi/4}\psi^{(u)}(\theta, 0) \tag{49}$$

However, a doubling occurs for the first time at 1/16 of the full revival time, $t/\pi = 4$.

In summary, it is observed that the number of maxima of the g and u densities in Fig. 6(a,b) is identical for all fractional revival times. Due to the different phase relationships between the two initial Gaussian packets, however, the positions of those maxima differ, giving rise to different patterns in the quantum carpets of $|\psi(\theta, t)|^2$. While for the even (g) wave functions all of the above relationships are equivalent to those for the single well pendulum but with $t \to t/4$ and $\theta \to \theta/2$, as implied by the scaling relation (4) for Mathieu's equation, the odd (u) dynamics shows completely different patterns.

The "quantum carpets" representing the evolving probability densities in the free rotor limit exhibit intriguing combinations of spatial and temporal structures. It can be seen in Fig. 6(a) that the even parity density exhibits linear canals at $\theta = \pm t, \pm 3t, \ldots$ and linear ridges at $\theta = 0, \pm t, \pm 2t, \pm 4t, \ldots$. An alternative set of such ridges is found for $\theta = \kappa t + \pi/2$ for all integer values of κ. The odd parity density plot in Fig. 6(b) is qualitatively different. The first class of rays intersects the abscissa at $\theta = 0, \pi$ featuring canals or ridges for even or odd slopes $d\theta/dt$. The most pronounced of the former ones are the vertical canals. Another class of rays intersects the abscissa at $\theta = \pi/2, 3\pi/2$, yielding ridges for all integer slopes. Finally, the situation for the initially localized wave packet displayed in Fig. 6(c) yields characteristic rays not only in places where the even or odd parity densities showed their rays, but also new rays that emerge from the interference of even and odd components. For an in-depth discussion of space-time structures and characteristic rays, the reader is referred to App. A.

Expression (45) for the evolving wavefunctions also allows for a ready evaluation of expectation values of observables of interest. For the double well situation with $m = 2$, we consider the degree of alignment, $\cos^2\theta$, instead of the degree of orientation, $\cos\theta$, because

the potential energy does not distinguish between $\theta = 0$ and $\theta = \pi$.

$$\begin{aligned}\langle\cos^2\theta\rangle^{(g)}(t) &= \int_0^{2\pi} |\psi^{(g)}(\theta,t)|^2\ \cos^2\theta\, d\theta \\ &= \frac{1}{2} + \frac{1}{2}A_0^{(g)}A_1^{(g)}\cos(2t) + \frac{1}{2}\sum_{n=0}^{\infty} A_n^{(g)}A_{n+1}^{(g)}\cos[(4n+2)t] \qquad (50a)\\ \langle\cos^2\theta\rangle^{(u)}(t) &= \int_0^{2\pi} |\psi^{(u)}(\theta,t)|^2\ \cos^2\theta\, d\theta \\ &= \frac{1}{2} - \frac{1}{4}\left(B_0^{(u)}\right)^2 + \frac{1}{2}\sum_{n=0}^{\infty} B_n^{(u)}B_{n+1}^{(u)}\cos[(4n+4)t] \qquad (50b)\end{aligned}$$

The result for the even parity (g) alignment is shown as a solid curve in Fig. 7 (a). The most obvious discrepancy from the single well orientation (29) displayed in Fig 3 (c) is that now the dynamics is four times faster while the frequency for the odd parity (u) state oscillates another two times faster. Starting from a highly aligned situation, $\langle\cos^2\theta\rangle^{(g/u)}(0) \approx 0$, the initial spreading quickly approaches the isotropic value of $\langle\cos^2\theta\rangle^{(g/u)} \approx 0.5$. In particular, the fractional revivals at $t/\pi = 1/4$ discussed above do not leave any fingerprint. At $t/\pi = 1/2$, the g state reaches its half revival time with the lobes of its wavefunction now residing at $\theta = 0, \pi$ leading to strong anti–alignment, $\langle\cos^2\theta\rangle^{(g)}(\pi/2) \approx 1$. In marked contrast, the u state reaches the 1/8 revival time where the wavefunction regains, apart from a global phase factor, its original shape thus leading to high alignment, $\langle\cos^2\theta\rangle^{(u)}(\pi/2) \approx 0$. After that event, the alignment signals for both g and u parity states approach the isotropic plateaux again, $\langle\cos^2\theta\rangle^{(g/u)} \approx 0.5$, before returning to a highly aligned state again, $\langle\cos^2\theta\rangle^{(g/u)}(0) \approx 0$. Note that this time corresponds to a full or a quarter revival for g or u state dynamics, respectively. Finally, it is noted that the transient alignment for the parity-less, initially localized wavefunction, $\psi^{(l)}$, follows that for the g and u functions near $t = 0$ and $t = \pi$ but stays near the isotropic value of 0.5 all the time in between.

As will be shown in App. B, the results (50) for the time dependence of the mean alignment can be expressed in terms of Mathieu function thus yielding the double well analog of Eq. (31).

$$\begin{aligned}\langle\cos^2\theta\rangle^{(g)}(t) &= \frac{1}{2} - \left(\frac{1}{2\pi\beta^2}\right)^{1/4}\exp\left(-\frac{1}{\beta^2}\right)\mathrm{se}_1\left(2t+\frac{\pi}{2};\frac{V}{8}\right) \qquad (51a)\\ \langle\cos^2\theta\rangle^{(u)}(t) &= \frac{1}{2} - \left(\frac{1}{2\pi\beta^2}\right)^{1/4}\exp\left(-\frac{1}{\beta^2}\right)\mathrm{ce}_0\left(2t+\frac{\pi}{2};\frac{V}{8}\right) \qquad (51b)\end{aligned}$$

where the harmonic oscillator limit of Mathieu functions (41) was used. This formulation allows for an easy calculation of the extrema of the alignment curves observed in Fig. 7 (a)

yielding $1-\langle\cos^2\theta\rangle^{(g/u)}(0,\pi)=\langle\cos^2\theta\rangle^{(g)}(\pi/2)\approx 0.9592$. While at its half revival time the g parity signal exactly passes the isotropic value, $\langle\cos^2\theta\rangle^{(g)}(\pi/4)=0.5$, this value is reached for the 1/8 revival of the u state only approximately. For the barrier height $V=100$ considered here, we find $\langle\cos^2\theta\rangle^{(u)}(0)\approx 0.4989$.

VI. SUMMARY

In this work the quantum dynamics of a plane pendulum is treated using a semi-analytic approach. It is based on expanding the solutions of the time-dependent Schrödinger equation in terms of Mathieu functions which appear as solutions of the time-independent Schrödinger equation [12]. Once the Fourier coefficients specifying the eigenvectors are obtained numerically, various quantum dynamical scenarios can be expressed analytically in terms of these coefficients. In particular, pendular analogues of the celebrated squeezed and coherent states of a harmonic oscillator are investigated. This is achieved by instantaneously changing the barrier height or by instantaneously shifting the trigonometric potential horizontally. Squeezed pendular states are discussed between the limiting case of the harmonic oscillator and the free rotor limit. Coherent pendular states are discussed between the limits of smallest displacements, in which case the quantum dynamics can be well described within the harmonic approximation, and the limit of largest possible displacement, i. e. the case of the inverted pendulum. In all those cases, semi-analytic expressions for the wave packet evolution as well as for the corresponding mean orientation or alignment are derived in terms of the above-mentioned Fourier coefficients. A special case is the free rotor dynamics starting from initial wave functions in the harmonic limit, i. e., narrow Gaussian packets evolving freely on a circle where simple expressions for the wave functions allow an analysis of temporal features (full and fractional revivals) and spatiotemporal features (quantum carpets). Furthermore, the mean orientation and alignment can be expressed as Mathieu functions in time. Novel features arise when passing on from the periodic single well potential to the pendular analogue of the double well potential. While the lowest states forming tunneling doublets in deep potential wells can hardly be distinguished by traditional, i. e. energy resolved, techniques, the time dependent approach pursued in this paper opens several routes to the separation of states of different parity: Full and fractional revivals occur at different times for even states, odd states, and localized superpositions thereof. Also the charac-

teristic rays (canals and ridges) are found at different locations in the respective quantum carpets. Furthermore, the different revival times and structures of the corresponding probability densities give rise to strong alignment or anti-alignment at certain instances in time, depending on the parity of the initial state.

In future work, the present approach could be extended in several directions: The first is the generalization to a spherical pendulum, where the representation of pendular states in terms of Mathieu functions (in one angular coordinate) has to be replaced by oblate spheroidal wave functions (in two angular degrees of freedom) [15, 48]. Another intriguing case is the investigation of periodic multi-well potentials, e. g. the intramolecular rotation of a methyl group with $m = 3$ [7, 22]. Instead of the concept of two parity states, there are m states transforming according to different irreducible representations of the point group of rotations. They are expected to show qualitatively different spatiotemporal densities yielding different experimentally observable, transient properties.

Acknowledgment

This research is funded by the project "*Analysis and control of ultrafast photoinduced reactions*" (SFB 450) of the Deutsche Forschungsgemeinschaft (DFG). We are grateful to J. C. Gutierrez Vega for providing us an efficient Matlab code for the numerical solution of Mathieu's equation.

APPENDIX A: SPACE-TIME STRUCTURES OF FREE ROTOR WAVE FUNCTIONS

In this appendix, the evolutions of the probability densities obtained in the free rotor limit of squeezed pendular states displayed in Figs. 2(c) and 6(a,b,c) for single well and double well potentials, respectively, shall be discussed in more detail. In addition to purely spatial patterns (nodal structures of wave functions) and purely temporal patterns (fractional revivals) already discussed above, interesting features arise from the combination of spatial and temporal structures, similar to those discussed for quantum carpets of a particle in a square well [34]. In particular, linear canals (minima) and linear ridges (maxima, interspersed with saddles) are found in the space-time representation of densities.

The time-dependent wave functions (25) and (45) for the free rotor limits of the single and double well case, respectively, are found to be of the general form

$$\begin{aligned}\psi(\theta,t) &= \frac{1}{\sqrt{\pi}}\sum_{\nu=0}^{\infty} C_\nu\, z^{\nu^2}\cos(\nu\theta-\mu\pi/2)\\ &= \frac{i^{-\mu}}{2\sqrt{\pi}}\sum_{\nu=0}^{\infty} C_\nu\left[z^{\nu^2}e^{i\nu\theta}+(-1)^\mu z^{\nu^2}e^{-i\nu\theta}\right]\end{aligned} \tag{A1}$$

with $z\equiv\exp(-it/2)$ and where C stands for the Fourier coefficients A or B characterizing the Mathieu functions, ν represents even, odd, or unrestricted positive integer numbers, and $\mu\in\{0,1\}$ is used to distinguish between cosine and sine elliptic wave functions. From the density plots in Fig. 2(c) and 6 it is apparent that the characteristic rays (canals and ridges) on which the extremal values of $|\psi(\theta,t)|$ can always be given by

$$\theta_{\kappa\lambda}(t)=(\kappa t+\lambda\pi)/2 \tag{A2}$$

with κ,λ being integer numbers. As already noted in Ref. [34], these rays can be interpreted as trajectories of free particles on a ring, starting at initial angles $\theta(0)=\lambda\pi/2$ and proceeding with quantized angular velocities $d\theta/dt=\kappa/2$ which are commensurate with a full revival time of 4π obtained for $\psi^{(0)}$, $\psi^{(u)}$, and $\psi^{(l)}$. Note that for the case of $\psi^{(g)}$ with a revival time of π, only even values of κ can occur as is indeed found below, see the scaling relation given in Eq. (4). Evaluating the wave functions along these rays yields

$$\psi_{\kappa\lambda}(t)=\frac{1}{2\sqrt{\pi}}\sum_{\nu=0}^{\infty} i^{\nu\lambda-\mu}C_\nu\left[z^{\nu(\nu-\kappa)}+(-1)^{\nu\lambda-\mu}\,z^{\nu(\nu+\kappa)}\right] \tag{A3}$$

Substituting $\nu+\kappa$ by ν in the second term renders the time-dependent phase-factors of the two summands identical

$$\psi_{\kappa\lambda}(t)=\frac{1}{2\sqrt{\pi}}\left[\sum_{\nu=0}^{\infty} i^{\nu\lambda-\mu}C_\nu z^{\nu(\nu-\kappa)}+\sum_{\nu=\kappa}^{\infty} i^{3(\nu\lambda-\kappa\lambda-\mu)}C_{\nu-\kappa}z^{\nu(\nu-\kappa)}\right] \tag{A4}$$

where the summation in the second term starts from $\nu=\kappa$. Due to the symmetry of the free rotor densities in Figs. 2 and 6 with respect to inversion at $\theta=\lambda\pi/2$, the rays with $\kappa<0$ are mirror images of those with $\kappa>0$. Hence, we shall restrict the following discussion to the case of $\kappa\geq 0$, thus allowing to separate the first $\kappa-1$ terms occurring only in the first summation from the remaining ones

$$\psi_{\kappa\lambda}(t)=\frac{1}{2\sqrt{\pi}}\left[\sum_{\nu=0}^{\kappa-1} i^{\nu\lambda-\mu}C_\nu z^{\nu(\nu-\kappa)}+\sum_{\nu=\kappa}^{\infty} i^{\nu\lambda-\mu}\left(C_\nu+i^{-3\kappa\lambda}(-1)^{\nu\lambda-\mu}C_{\nu-\kappa}\right)z^{\nu(\nu-\kappa)}\right] \tag{A5}$$

While the time-dependent phase factors (powers of q) rotate in the complex plane giving rise to rich interference phenomena, the time-independent pre-factors govern the amplitude of the oscillations. They shall be analyzed in the following, for individual rays specified by the values κ, λ, for specific types of wavefunctions specified by their multiplicity m, parity μ, and corresponding Fourier coefficients C_ν. In particular, the sign structure of the latter shall prove useful.

1. Single well

Comparing expression (25) for the free rotor limit for the single well wavefunction with the present ansatz (A1), one readily identifies the Fourier coefficients $C_\nu = A_\nu^{(0)}$ with $\nu = n$ for the pendular ground state which is a cosine elliptic function ($\mu = 0$). The corresponding density plot in Fig. 2(c) shows characteristic rays as defined in Eq. (A2) for all integer numbers κ and for $\lambda = 0, 4, \ldots$. Thus, the exponents $\nu\lambda - \mu$ and $3\kappa\lambda$ are multiples of four rendering all time-independent phase factors unity and Eq. (A5) simplifies to

$$\psi_{\kappa\lambda}^{(0)}(t) = \frac{1}{2\sqrt{\pi}} \left[\sum_{n=0}^{\kappa-1} A_n^{(0)} z^{n(n-\kappa)} + \sum_{n=\kappa}^{\infty} \left(A_n^{(0)} + A_{n-\kappa}^{(0)} \right) z^{n(n-\kappa)} \right] \tag{A6}$$

If the initial wavefunction $\phi_0(\theta)$ is sufficiently narrow ($E_0 \ll V$), the harmonic approximation (12) can be invoked. Due to the alternating sign structure of the coefficients $A_n^{(0)}$, the sum $A_n^{(0)} + A_{n-\kappa}^{(0)}$ is large for even values of κ while it becomes small for odd values of κ. In particular, in the limit of $\beta \to \infty$, the Gaussian shaped distribution (12) becomes infinitely wide and the sum $A_n^{(0)} + A_{n-\kappa}^{(0)}$ goes to zero (canals) or to $2A_n^{(0)}$ (ridges) for odd or even values of κ, respectively. In that limit, also the magnitude of the first sum in (A6) tends to zero. Thus, the density along the odd order rays goes to zero in the limit of $\beta \to \infty$. In contrast, for finite values of β, the alternating canals and ridges become less pronounced for increasing κ. Another class of characteristic rays is observed for $\lambda = 2$ and arbitrary integer κ. Here, the bracket in front of the second exponential in (A6) reads $(A_n^{(0)} + (-1)^\kappa A_{n-\kappa}^{(0)})$ which approaches $2A_n^{(0)}$ in the harmonic limit, thus explaining the ridges observed for both for even and odd orders κ.

Note that all these considerations do not hold for the general case, i. e., without the assumption of an initially narrow Gaussian. As shown in Ref. [18], the alternating sign structure of the Fourier coefficients is only found for higher order coefficients, while the

lower ones have equal sign.

2. Double well

First, let us consider the free rotor limit for the even parity ($\mu = 0$) double well wavefunction (45a). Comparison with Eq. (A1) yields coefficients $C_\nu = A^{(g)}_{\nu/2}$ with even indices $\nu = 2n$. The corresponding density plot in Fig. 6(a) exhibits characteristic rays for both κ and λ being even numbers. Again, the exponents $\nu\lambda - \mu$ and $3\kappa\lambda$ are multiples of four rendering all time-independent phase factors unity yielding a result similar to Eq. (A6) for single well pendular states

$$\psi^{(g)}_{\kappa\lambda}(t) = \frac{1}{2\sqrt{\pi}} \left[\sum_{n=0}^{\kappa/2-1} A^{(g)}_n z^{2n(2n-\kappa)} + \sum_{n=\kappa/2}^{\infty} \left(A^{(g)}_n + A^{(g)}_{n-\kappa/2} \right) z^{2n(2n-\kappa)} \right] \tag{A7}$$

Also in this case the corresponding harmonic approximation (41) has an alternating sign structure of the Fourier coefficients, with vanishing difference of the magnitude of neighboring coefficients in the limit of $\beta \to \infty$. Hence, canals are found for $\kappa = 2, 6, \ldots$ and ridges for $\kappa = 0, 4, 8, \ldots$. An alternative set of characteristic rays is found for odd values of λ and even values of κ. In this case, the bracket changes to $(A^{(g)}_n + (-1)^{\kappa/2} A^{(g)}_{n-\kappa/2})$ which gives rise to the ridges observed for all even orders κ in the harmonic limit. Note again that the complete space–time structure is equivalent to the single well case but with scaled angle ($\theta \to 2\theta$) and scaled time ($t \to 4t$), as noted previously in Secs. II and V.

A qualitatively different situation is encountered for the wave packet evolution starting from the odd parity ($\mu = 1$) member of the ground tunneling doublet, see Eq. (45b). Now the coefficients can be identified to be $C_\nu = B^{(u)}_{(\nu-1)/2}$ with odd indices $\nu = 2n + 1$. The corresponding density plot in Fig. 6(b) shows a variety of characteristic rays but only for even values of κ. The first class of rays is found for even λ where the pre-factor of the second exponential function in Eq. (A5) reduces to $(B^{(u)}_n - B^{(u)}_{n-\kappa/2})$ yielding canals or ridges for even or odd values of $\kappa/2$, respectively. Most pronounced are the vertical canals ($\kappa = 0$) where the wave function is exactly zero, in accordance with the odd parity which is conserved for all times. The second class of rays is found for odd λ, in which case the pre-factor reduces to $(B^{(u)}_n + (-1)^{\kappa/2} B^{(u)}_{n-\kappa/2})$ resulting in ridges for all even values of κ, due to the oscillating sign structure in the harmonic limit of B_n, see Eq. (41).

Finally, the situation for a wave packet initially localized in one of the potential wells shall be discussed. First of all, Fig. 6(c) indicates that characteristic rays exist only for odd values of λ. A first set of ridges is found for even values of κ, both for $\lambda = 1$ and for $\lambda = 3$. It is obvious that their existence is straightforward to derive from the existence of identical rays in the time evolution of even and odd parity states as discussed above. This is, however, not true for the other set of ridges observed for odd values of κ. For a quantitative explanation of their occurrence, let us consider Eq. (A3) and insert definition (45) which yields

$$\begin{aligned}\psi_{\kappa\lambda}^{(l)}(t) &= \frac{1}{2\sqrt{2\pi}}\sum_{\nu=0}^{\infty}(-1)^{n\lambda}A_n^{(g)}\left[z^{2n(2n-\kappa)}+z^{2n(2n+\kappa)}\right] \\ &+ \frac{i^{\lambda-1}}{2\sqrt{2\pi}}\sum_{\nu=0}^{\infty}(-1)^{n\lambda}B_n^{(u)}\left[z^{(2n+1)(2n+1-\kappa)}+(-1)^{\lambda-1}\,z^{(2n+1)(2n+1+\kappa)}\right] \qquad \text{(A8)}\end{aligned}$$

for the time evolution of the wave function along the characteristic rays. Replacing n by $n-(\kappa-1)/2$ in the upper right parts of the equation, and n by $n-(\kappa+1)/2$ in the lower right, and grouping together terms with equal powers of z finally yields

$$\begin{aligned}\psi_{\kappa\lambda}^{(l)}(t) &= \frac{1}{2\sqrt{2\pi}}\sum_{n=0}^{\kappa^-}(-1)^{n\lambda}A_n^{(g)}z^{2n(2n-\kappa)} \\ &+ \frac{1}{2\sqrt{2\pi}}\sum_{n=\kappa^+}^{\infty}(-1)^{n\lambda}\left[A_n^{(g)}+i^{3(\lambda-1)}(-1)^{-\lambda\kappa^+}B_{n-\kappa^+}^{(u)}\right]z^{2n(2n-\kappa)} \\ &+ \frac{i^{\lambda-1}}{2\sqrt{2\pi}}\sum_{n=0}^{\kappa^--1}(-1)^{n\lambda}B_n^{(u)}z^{(2n+1)(2n+1-\kappa)} \\ &+ \frac{1}{2\sqrt{2\pi}}\sum_{n=\kappa^-}^{\infty}(-1)^{n\lambda}\left[(-1)^{-\lambda\kappa^-}A_{n-\kappa^-}^{(g)}+i^{\lambda-1}B_n^{(u)}\right]z^{(2n+1)(2n+1-\kappa)} \qquad \text{(A9)}\end{aligned}$$

where $\kappa^{\pm}=(\kappa\pm1)/2$ are integer numbers for odd values of κ. In the following we shall treat the cases $\lambda = 1$ and $\lambda = 3$ separately: First, let us consider the case of rays starting from the center of the initial wave packet ($\lambda = 1$). The square brackets in the second and fourth summation in the last equation reduce to $[A_n^{(g)}+(-1)^{\kappa^+}B_{n-\kappa^+}^{(u)}]$ and $[(-1)^{\kappa^-}A_{n-\kappa^-}^{(g)}+B_n^{(u)}]$, respectively. Inserting the harmonic limit (41), it is evident from the equal signs of Fourier coefficients $A_n^{(g)}$ and $B_n^{(u)}$ that the space-time representation of the densities must have ridges. Note that we previously also showed the presence of ridges for even κ. Hence, for $\lambda = 1$ there are ridges for all integer values of κ, with no canals in between. Finally, we consider rays starting opposite of the initial wave packet ($\lambda = 3$). In that case, the two brackets yield

$[A_n^{(g)} - (-1)^{\kappa^+} B_{n-\kappa^+}^{(u)}]$ and $[(-1)^{\kappa^-} A_{n-\kappa^-}^{(g)} - B_n^{(u)}]$ yielding canals for odd values of κ. They are interspersed by the ridges for even values of κ as discussed earlier.

APPENDIX B: FREE ROTOR LIMIT OF MEAN VALUES

In this appendix we show that the mean orientation or alignment of a squeezed pendular state in the free rotor limit can be expressed as Mathieu elliptic functions in time if the Mathieu coefficients of the initial wave function are given in the harmonic limit. For the following derivation, we recall that for Mathieu functions with $m = 1$ (single well)

$$A_n^{(0)} = A_n^{(0)}(q = 2V) \tag{B1a}$$

$$B_n^{(1)} = B_n^{(1)}(q = 2V) \tag{B1b}$$

as defined in Eqs. (2) and (6). In the harmonic oscillator limit, Eq. (10), we define the parameter $\beta = (V/2)^{1/4}$ and can also write

$$q = 4\beta^4. \tag{B2}$$

For Mathieu functions with $m = 2$ (double well), the Fourier coefficients are given as

$$A_n^{(g)} = A_n^{(g)}(q = V/2) \tag{B3a}$$

$$B_n^{(u)} = B_n^{(u)}(q = V/2)\,. \tag{B3b}$$

In the harmonic oscillator limit, Eq. (40), with $\beta = (2V)^{1/4}$ this leads to

$$q = \frac{\beta^4}{4}. \tag{B4}$$

1. Single well pendulum

We start with expression (29) for the mean orientation of a squeezed state in the free rotor limit for a single well potential. If one inserts he harmonic approximation (11) for the Fourier coefficients of the ground vibrational state $A_k^{(0)}$, one obtains the analytical expression

$$\langle \cos\theta \rangle^{(0)}(t) = -\frac{2N_0^2}{\beta^2} \sum_{n=0}^{\infty} \exp\left[-\frac{2n^2+2n+1}{2\beta^2}\right] \cos\left[(2n+1)\frac{t}{2}\right] \tag{B5}$$

Expressing the cosine by a shifted sine-function, this can also be written as

$$\langle\cos\theta\rangle^{(0)}(t) = \frac{2N_0^2}{\beta^2}\exp\left(-\frac{1}{4\beta^2}\right) \tag{B6}$$

$$\times \sum_{n=0}^{\infty}\exp\left(-\frac{(2n+1)^2}{4\beta^2}\right)(-1)^n\sin\left[(2n+1)\left(\frac{t}{2}-\frac{\pi}{2}\right)\right]. \tag{B7}$$

Comparing (B7) with the Fourier coefficients of the lowest Mathieu sine elliptic function, Eq. (41c), one obtains

$$\langle\cos\theta\rangle^{(0)}(t) = 2^{1/4}\frac{N_0}{\beta}\exp\left(-\frac{1}{4\beta^2}\right)\sum_{n=0}^{\infty}\hat{B}_n^{(u)}\sin\left[(2n+1)\left(\frac{t}{2}-\frac{\pi}{2}\right)\right]. \tag{B8}$$

Here, according to (B4) the Fourier coefficients are,

$$\hat{B}_n^{(u)} = \hat{B}_n^{(u)}\left(\hat{q}=\hat{\beta}^4/4\right) \quad \text{with} \quad \hat{\beta} = \sqrt{2}\beta = (2V)^{1/4}. \tag{B9}$$

Using the normalization (11)

$$\hat{N}_0 = \left(\frac{\hat{\beta}^2}{\pi}\right)^{1/4} \tag{B10}$$

and the Mathieu expansion (38b) of odd parity states in a double well, we can finally write

$$\langle\cos\theta\rangle^{(0)}(t) = \left(\frac{2}{\pi\beta^2}\right)^{1/4}\exp\left(-\frac{1}{4\beta^2}\right)\mathrm{se}_1\left(\frac{t-\pi}{2},\frac{V}{2}\right). \tag{B11}$$

Hence, we have shown that, for a single well potential, the mean orientation can be written as the lowest Mathieu sine elliptical function in time, shifted by $\pi/2$ with the argument $\hat{q} = V/2$.

2. Double well

For a double well potential, the mean alignment of the even and odd wave functions can be expressed in a similar way. Starting from Eq. (50), we can insert the harmonic oscillator limit (41) for the coefficients $A_n^{(g)}$ and $B_n^{(u)}$ and obtain

$$\langle\cos^2\theta\rangle^{(g)}(t) = \frac{1}{2} - 2\frac{N_0^2}{\beta^2}\sum_{n=0}^{\infty}\exp\left(-\frac{4n^2+4n+2}{\beta^2}\right)\cos\left[(4n+2)t\right] \tag{B12a}$$

$$\langle\cos^2\theta\rangle^{(u)}(t) = \frac{1}{2} - \frac{N_0^2}{\beta^2}\exp\left(-\frac{1}{\beta^2}\right)$$

$$- 2\frac{N_0^2}{\beta^2}\sum_{n=0}^{\infty}\exp\left(-\frac{4n^2+8n+5}{\beta^2}\right)\cos\left[(4n+4)t\right]. \tag{B12b}$$

By replacing the cosine by shifted sine or cosine functions for the even and odd wave functions, respectively, this can be rewritten as

$$\begin{aligned}\langle\cos^2\theta\rangle^{(g)}(t) &= \frac{1}{2} - 2\frac{N_0^2}{\beta^2}\exp\left(-\frac{1}{\beta^2}\right)\sum_{n=0}^{\infty}(-1)^n\exp\left(-\frac{(2n+1)^2}{\beta^2}\right)\\ &\times \sin\left[(2n+1)\left(2t+\frac{\pi}{2}\right)\right] \qquad \text{(B13a)}\\ \langle\cos^2\theta\rangle^{(u)}(t) &= \frac{1}{2} - \frac{N_0^2}{\beta^2}\exp\left(-\frac{1}{\beta^2}\right) - 2\frac{N_0^2}{\beta^2}\exp\left(-\frac{1}{\beta^2}\right)\\ &\times \sum_{n=1}^{\infty}(-1)^n\exp\left(-\frac{4n^2}{\beta^2}\right)\cos\left[2n\left(2t+\frac{\pi}{2}\right)\right]. \qquad \text{(B13b)}\end{aligned}$$

Note that, for the odd wave function, we have also shifted the summation index from $n+1$ to n, so that the sum starts from $n=1$. Comparing the last two equations with Eq. (41) leads to

$$\langle\cos^2\theta\rangle^{(g)}(t) = \frac{1}{2} - \frac{1}{2^{1/4}}\frac{N_0}{\beta}\exp\left(-\frac{1}{\beta^2}\right)\sum_{n=0}^{\infty}\check{B}_k^{(u)}\sin\left[(2n+1)\left(2t+\frac{\pi}{2}\right)\right] \qquad \text{(B14)}$$

and Eqs.(B3) and (B4) allow to identify the coefficients as

$$\check{B}_k^{(u)} = \check{B}_k^{(u)}\left(\check{q}=\frac{\check{\beta}^4}{4}=\frac{V}{8}\right) \quad \text{with} \quad \check{\beta}=\beta/\sqrt{2}. \qquad \text{(B15)}$$

Similarly, for the odd wave function, we can write

$$\langle\cos^2\theta\rangle^{(u)}(t) = \frac{1}{2} - \frac{1}{2^{1/4}}\frac{N_0}{\beta}\exp\left(-\frac{1}{\beta^2}\right)\sum_{n=0}^{\infty}\check{A}_k^{(g)}\cos\left[2n\left(2t+\frac{\pi}{2}\right)\right] \qquad \text{(B16)}$$

with

$$\check{A}_k^{(g)} = \check{A}_k^{(g)}\left(\check{q}=\frac{\check{\beta}^4}{4}=\frac{V}{8}\right). \qquad \text{(B17)}$$

Note, that the second term on the r. h. s. of Eq. (B13b) is combined with the sum over n, which now starts from $n=0$. Finally, we can use expansion (38) of the Mathieu functions in terms of cosine and sine functions and obtain

$$\begin{aligned}\langle\cos^2\theta\rangle^{(g)}(t) &= \frac{1}{2} - \left(\frac{1}{2\pi\beta^2}\right)^{1/4}\exp\left(-\frac{1}{\beta^2}\right)\mathrm{se}_1\left(2t+\frac{\pi}{2};\frac{V}{8}\right) \qquad \text{(B18a)}\\ \langle\cos^2\theta\rangle^{(u)}(t) &= \frac{1}{2} - \left(\frac{1}{2\pi\beta^2}\right)^{1/4}\exp\left(-\frac{1}{\beta^2}\right)\mathrm{ce}_0\left(2t+\frac{\pi}{2};\frac{V}{8}\right). \qquad \text{(B18b)}\end{aligned}$$

We have shown that, depending on the symmetry of the wave function, the mean alignment can be written as the lowest Mathieu sine or cosine elliptic functions in time, shifted by $\pi/2$

in the angular argument and for the parameter $\breve{q} = V/8$. Again, it is noted that the result (B18a) for the even wave function is equivalent to that for the single well pendulum, by virtue of $\cos^2\theta = [1 + cos(2\theta)]/2)$ and the scaling relation given in Eq. (4).

---

[1] H. J. Loesch, Ann. Rev. Phys. Chem. **46**, 555 (1995), URL http://dx.doi.org/10.1146/annurev.pc.46.100195.003011.

[2] B. Friedrich and D. Herschbach, Nature **353**, 412 (1991), URL http://dx.doi.org/10.1038/353412a0.

[3] B. Friedrich and D. Herschbach, Phys. Rev. Lett. **74**, 4623 (1995), URL http://dx.doi.org/10.1103/PhysRevLett.74.4623.

[4] T. Seideman, J. Chem. Phys. **103**, 7887 (1995), URL http://dx.doi.org/10.1063/1.470206.

[5] T. Seideman and E. Hamilton, Adv. At. Mol. Opt. Phys. **52**, 289 (2006).

[6] S. Ramakrishna and T. Seideman, Phys. Rev. Lett. **99**, 103001 (2007), URL http://dx.doi.org/10.1103/PhysRevLett.99.103001.

[7] G. L. Baker, J. A. Blackburn, and H. J. T. Smith, Am. J. Phys. **70**, 525 (2002), URL http://dx.doi.org/10.1119/1.1456069.

[8] R. Graham, M. Schlautermann, and P. Zoller, Phys. Rev. A **45**, R19 (1992), URL http://dx.doi.org/10.1103/PhysRevA.45.R19.

[9] H. Ammann, R. Gray, I. Shvarchuck, and N. Christensen, Phys. Rev. Lett. **80**, 4111 (1998), URL http://dx.doi.org/10.1103/PhysRevLett.80.4111.

[10] F. L. Moore, J. C. Robinson, C. F. Bharucha, and M. G. Raizen, Phys. Rev. Lett. **75**, 4598 (1995).

[11] M. Leibscher and I. S. Averbukh, Phys. Rev. A **65**, 053816 (2002), URL http://dx.doi.org/10.1103/PhysRevA.65.053816.

[12] E. U. Condon, Phys. Rev. **31**, 891 (1928), URL http://dx.doi.org/10.1103/PhysRev.31.891.

[13] G. L. Baker and J. A. Blackburn, *The Pendulum: A Case Study in Physics* (Oxford University Press, Oxford, 2005).

[14] E. Mathieu, J. Math Pures Appl. **13**, 137 (1868).

[15] M. Abramovitz and I. Stegun, *Handbook of Mathematical Functions* (Dover, New York, 1972).

[16] I. S. Gradshteyn and I. M. Ryzhik, *Tables of Integrals, Series, and Products* (Academic, New York, 1980).

[17] J. C. Gutierrez-Vega, R. M. Rodriguez-Dagnino, M. A. Meneses-Nava, and S. Chavez-Cerda, Am. J. Phys. **71**, 233 (2003), URL http://dx.doi.org/10.1119/1.1522698.

[18] J. C. Gutierrez-Vega (2003), URL http://homepages.mty.itesm.mx/jgutierr/Mathieu.html.

[19] T. Pradhan and A. V. Khare, Am. J. Phys. **41**, 59 (1973), URL http://dx.doi.org/10.1119/1.1987121.

[20] G. P. Cook and C. S. Zaidins, Am. J. Phys **54**, 259 (1986), URL http://dx.doi.org/10.1119/1.14640.

[21] R. Bluhm, V. A. Kostelecký, and J. A. Porter, Am. J. Phys. **64**, 944 (1996), URL http://dx.doi.org/10.1119/1.18304.

[22] R. M. Dimeo, Am. J. Phys. **71**, 885 (2003), URL http://dx.doi.org/10.1119/1.1538575.

[23] M. A. Doncheski and R. W. Robinett, Annals of Physics **308**, 578 (2003), URL http://dx.doi.org/10.1016/S0003-4916(03)00171-4.

[24] E. Schrödinger, Naturwiss. **14**, 664 (1926).

[25] R. J. Glauber, Phys. Rev. **131**, 2766 (1963), URL http://dx.doi.org/10.1103/PhysRev.131.2766.

[26] W. P. Schleich, *Quantum Optics in Phase Space* (Wiley–VCH, Berlin, 2001).

[27] J. Parker and C. R. Stroud, Phys. Rev. Lett. **56**, 716 (1986), URL http://dx.doi.org/10.1103/PhysRevLett.56.716.

[28] I. S. Averbukh and N. F. Perelman, Phys. Lett. A **139**, 449 (1989).

[29] J. A. Yeazell, M. Mallalieu, and C. R. Stroud, Phys. Rev. Lett. **64**, 2007 (1986), URL http://dx.doi.org/10.1103/PhysRevLett.64.2007.

[30] C. Leichtle, I. S. Averbukh, and W. P. Schleich, Phys. Rev. Lett. **77**, 3999 (1996), URL http://dx.doi.org/10.1103/PhysRevLett.77.3999.

[31] C. Leichtle, I. S. Averbukh, and W. P. Schleich, Phys. Rev. A **54**, 5299 (1996), URL http://dx.doi.org/10.1103/PhysRevA.54.5299.

[32] R. W. Robinett, Am. J. Phys. **68**, 410 (2000), URL http://dx.doi.org/10.1119/1.19455.

[33] P. Stifter, C. Leichtle, W. P. Schleich, and J. Markloff, Z. Naturforsch. **52 A** (1997).

[34] F. Grossmann, J.-M. Rost, and W. P. Schleich, J. Phys. A: Math. Gen. **30**, L277 (1997), URL http://dx.doi.org/10.1088/0305-4470/30/9/004.

[35] S. Fleischer, I. S. Averbukh, and Y. Prior, Phys. Rev. Lett. **99**, 093002 (2007), URL http://dx.doi.org/10.1103/PhysRevLett.99.093002.

[36] O. Deeb, M. Leibscher, J. Manz, W. von Muellern, and T. Seideman, ChemPhysChem **8**, 322 (2007), URL http://dx.doi.org/10.1002/cphc.200600543.

[37] H. Stapelfeldt and T. Seideman, Rev. Mod. Phys. **75**, 543 (2003), URL http://dx.doi.org/10.1103/RevModPhys.75.543.

[38] J. G. Underwood, M. Spanner, M. Y. Ivanov, J. Mottershead, B. J. Sussman, and A. Stolow, Phys. Rev. Lett. **90**, 223001 (2003), URL http://dx.doi.org/10.1103/PhysRevLett.90.223001.

[39] M. Muramatsu, M. Hita, S. Minemoto, and H. Sakai, Phys. Rev. A **79**, 011403 (2009), URL http://dx.doi.org/10.1103/PhysRevA.79.011403.

[40] R. Meyer, J. Chem. Phys. **52**, 2053 (1970), URL http://dx.doi.org/10.1063/1.1673259.

[41] C. C. Marston and G. G. Balint-Kurti, J. Chem. Phys. **91**, 3571 (1989), URL http://dx.doi.org/10.1063/1.456888.

[42] B. Friedrich and D. Herschbach, J. Phys. Chem. A **103**, 10280 (1999), URL http://dx.doi.org/10.1021/jp992131w.

[43] D. Tannor, *Introduction to Quantum Mechanics. A Time-Dependent Perspective* (University Science Books, Sausalito, 2004).

[44] C. Cohen-Tannoudji, B. Liu, and F. Laloe, *Quantum Mechanics* (Wiley, New York, 1977).

[45] J. Manz, B. Proppe, and B. Schmidt, Phys. Chem. Chem. Phys. **4**, 1876 (2002), URL http://dx.doi.org/10.1039/b109488b.

[46] Y. Fujimura, L. González, D. Kröner, J. Manz, I. Mehdaoui, and B. Schmidt, Chem. Phys. Lett. **386**, 248 (2004), URL http://dx.doi.org/10.1016/j.cplett.2004.01.070.

[47] B. G. Levine and T. J. Martínez, Annu. Rev. Phys. Chem. **58**, 613 (2007), URL http://dx.doi.org/10.1146/annurev.physchem.57.032905.104612.

[48] B. Friedrich and D. Herschbach, J. Phys. Chem. **99**, 15686 (1995), URL http://dx.doi.org/10.1021/j100042a051.